Physics of Plasmas

Effects of the guide field on electron distribution functions in the diffusion region of asymmetric reconnection

Cite as: Phys. Plasmas **26**, 082310 (2019); https://doi.org/10.1063/1.5092809
Submitted: 14 February 2019 . Accepted: 29 July 2019 . Published Online: 28 August 2019

N. Bessho, L.-J. Chen, S. Wang, and M. Hesse

COLLECTIONS

This paper was selected as Featured

View Online Export Citation CrossMark

ARTICLES YOU MAY BE INTERESTED IN

Whistler modes excited by magnetic antennas: A review
Physics of Plasmas **26**, 080501 (2019); https://doi.org/10.1063/1.5097852

Particle acceleration and fast magnetic reconnection
Physics of Plasmas **26**, 082112 (2019); https://doi.org/10.1063/1.5094179

Ion-neutral decoupling in the nonlinear Kelvin–Helmholtz instability: Case of field-aligned flow
Physics of Plasmas **26**, 082902 (2019); https://doi.org/10.1063/1.5103248

© 2019 Author(s).

Physics of Plasmas ARTICLE scitation.org/journal/php

Effects of the guide field on electron distribution functions in the diffusion region of asymmetric reconnection

Cite as: Phys. Plasmas **26**, 082310 (2019); doi: 10.1063/1.5092809
Submitted: 14 February 2019 · Accepted: 29 July 2019 ·
Published Online: 28 August 2019

View Online Export Citation CrossMark

N. Bessho,[1,2,a)] L.-J. Chen,[2] S. Wang,[1,2] and M. Hesse[3]

AFFILIATIONS

[1]Department of Astronomy, University of Maryland, College Park, Maryland 20742, USA
[2]Heliophysics Science Division, NASA Goddard Space Flight Center, Maryland 20771, USA
[3]Birkeland Centre for Space Science, University of Bergen, Bergen, Norway and Southwest Research Institute, San Antonio, Texas 78228, USA

[a)]naoki.bessho@nasa.gov

ABSTRACT

Crescent electron distribution functions in the electron diffusion region in asymmetric reconnection with a guide field (strength less than 50% of the upstream magnetic field) are investigated by theory and fully kinetic simulations. Electron motion in the electron diffusion region is a combination of meandering across the current sheet and gyration around the guide field. Combining the two canonical momentum conservation laws in a one-dimensional model with the energy conservation law, we derive the shape of crescent electron distribution functions in both velocity planes: perpendicular to the magnetic field and coplanner with the magnetic field. There are two major effects of the guide field on crescent distribution functions: (1) widening the opening angle of the crescent in a reduced distribution function and (2) the linear cut-off of a distribution function nonparallel to the magnetic field. We also discuss a translational mapping (perpendicular to the linear cut-off) of distribution functions between the X-line and another position. In addition, considering the gyration due to the normal magnetic field, we predict the shape of distribution functions in general positions in the electron diffusion region. The predictions will be useful to identify features of magnetic reconnection in a guide field by satellite observations.

Published under license by AIP Publishing. https://doi.org/10.1063/1.5092809

I. INTRODUCTION

Nongyrotropic electrons play important roles in the electron diffusion region (EDR) during magnetic reconnection. The nongyrotropy can arise due to meandering motion of particles in the reconnecting component of the magnetic field, which reverses its sign across a current sheet. Those meandering electrons are responsible for generating off-diagonal components of the electron pressure tensor, and the divergence of which can break the magnetic field lines in the EDR to change the topology of the magnetic field and convert magnetic energy into particle energy. Because of the meandering across the current sheet, electron velocity distribution functions (VDFs) in the EDR exhibit a characteristic crescent shape in the velocity plane perpendicular to the reconnecting magnetic field.[1–8] Recent space observations by NASA's Magnetospheric Multiscale (MMS) have detected the evidence of crescent electrons in magnetic reconnection at Earth's magnetopause.[9–18]

In our previous study of asymmetric reconnection without a guide field,[2] we obtained an equation to describe the parabolic boundary of a crescent electron VDF. The crescent part becomes outstanding in the magnetospheric side of the EDR, because the in-plane Hall electric field, which is highly enhanced in the magnetospheric side of the EDR, energizes meandering electrons. Depending on the distance from the magnetic neutral line, the opening angle of the crescent shape varies; the further the distance from the neutral line, the larger the opening angle of the crescent. In addition to the energization by the in-plane electric field, there is acceleration by the out-of-plane, reconnection electric field, which introduces the broadening of the crescent in the direction of acceleration. We derived an equation to determine the outer boundary of the crescent, which is given as a function of the number denoting how many times electrons cross the current sheet.[6] As the meandering continues in the EDR, the outermost boundary of the crescent is shifted toward the direction of electron acceleration by the reconnection electric field.

Crescent electron VDFs have been also studied in guide field reconnection. References 19 and 20 demonstrated by two-dimensional

Published under license by AIP Publishing

(2-D) particle-in-cell (PIC) simulations of guide field asymmetric reconnection that crescent electron VDFs are seen in the EDR in the velocity plane perpendicular to the magnetic field, and the guide field strength B_G in those studies is $B_G = B_0$, where B_0 is the asymptotic value of the reconnecting component of the magnetic field. Crescent electrons were observed in Ref. 13 in guide field reconnection, in which the guide field is $B_G \sim B_0$, in Earth's magnetopause by MMS observations, and in the velocity plane perpendicular to the magnetic field. Asymmetric reconnection was studied in Ref. 14 in Earth's magnetopause by MMS observations and 2-D PIC simulations, and crescent VDFs were detected in the EDR in reconnection with an intermediate-strength guide field, $B_G \sim 0.2B_0$. Also, it was shown by test particles that electron orbits are combined motion of meandering and gyration around a guide field. The study in Ref. 8 applied 2-D PIC simulations to show that electron crescent VDFs form up to the guide field $B_G \sim B_0$, but they do not form in reconnection with a stronger guide field, $B_G \sim 5B_0$.

Despite intensive studies of electron crescent VDFs in asymmetric reconnection, there has been no theory to explain the details of VDFs in the EDR during guide field reconnection. In this paper, we discuss the effects of the guide field on crescent electron VDFs during asymmetric magnetic reconnection by means of theory and kinetic simulations. As far as we know, this is the first study to derive analytical expressions of the shape of crescent VDFs in guide field reconnection. We consider the intermediate magnitude of the guide field, less than 50% of the asymptotic reconnecting magnetic field, in which electrons are still not fully magnetized in the EDR, and both meandering motion and gyration around the guide field are important.

The guide field modifies the shape of crescent VDFs. We will discuss three effects of the guide field on crescent electrons: widening of the opening angle of the crescent in a reduced VDF, a new VDF linear cut-off nonparallel to the magnetic field, and a translational VDF mapping perpendicular to the linear VDF cut-off from the X-line to a different location in the EDR. In addition to those guide field effects, we will extend the theory to explain VDFs in general positions around the X-line in both inflow and outflow directions.

The following is the organization of this paper: in Sec. II, we will explain simulation parameters and show some 2-D PIC simulation results. In Sec. III, we will describe the electron motion in the EDR in guide field reconnection, and we will derive several theoretical predictions for electron crescent VDFs. In Sec. IV, we will extend the theory discussed in Sec. III to general positions in the EDR. Section V gives conclusions of this study.

II. 2-D PIC SIMULATIONS OF ASYMMETRIC RECONNECTION WITH GUIDE FIELDS

Simulations are done in the x-y-z coordinates, where z is the current sheet normal direction, y is the direction of the current, and x is the direction of the reconnecting magnetic field across the current sheet. The initial magnetic field and density at $t=0$ are $B_x = B_0[\tanh(z/w) + \alpha_1]$ and $n = n_0[1 - \alpha_2 - \alpha_2\tanh(z/w) - (\alpha_2/2\alpha_1)\mathrm{sech}^2(z/w)]$, where B_0 is the mean asymptotic field between the magnetosheath, $(5/6)B_0$, and the magnetosphere, $(7/6)B_0$, with $\alpha_1 = 1/6$ and $\alpha_2 = 7/16$, n_0 is the sheath density, and the magnetosphere density is $n_0/8$. The current sheet width $w = 0.5d_i$, where $d_i = c/(n_0e^2/\epsilon_0 m_i)^{1/2}$ is the ion skin depth based on n_0, the speed of light c, the elementary charge e, the vacuum permittivity ϵ_0, and the ion mass m_i. Two conditions $v_{di}/v_{de} = -T_i/T_e$ and $B_0^2/2\mu_0 = n_0(T_i + T_e)(\alpha_2/2\alpha_1)$ are satisfied initially, where T_j and v_{dj} are temperature and a y-directed drift speed, respectively, a subscript $j = i$ or e represents the ion or electron species, and μ_0 is the vacuum permeability. A guide field is chosen as $B_y = B_G = 0.1B_0$, $0.2B_0$, $0.3B_0$, and $0.4B_0$, and in this paper, we denote each run as run 1 ($B_G = 0.1B_0$), run 2 ($B_G = 0.2B_0$), run 3 ($B_G = 0.3B_0$), and run 4 ($B_G = 0.4B_0$). To maximize the reconnection rate, we rotate the system clockwise in the x-y plane such that the new y direction bisects the angle between the asymptotic magnetic fields on the two sides, which is discussed in Eq. (7) of Ref. 21. For example, when $B_G = 0.2B_0$, the rotation angle is 1.88 degrees. In the following, all the data are shown in the rotated coordinates, and to describe the guide field in the rotated system, we use a subscript "g" as B_g, and to denote the guide field in the original nonrotated frame, we use a subscript "G" as B_G. To initiate reconnection, a perturbation to the magnetic flux function is added as $\Psi_1 = 0.1d_iB_0\mathrm{sech}^2(x/2w)\mathrm{sech}^2(z/w)$. The mass ratio of ion to electron $m_i/m_e = 25$, the temperature ratio $T_i/T_e = 2$, and the ratio of the plasma frequency to the electron cyclotron frequency $\omega_{pe}/\Omega_e = 4.0$, where $\omega_{pe} = (n_0e^2/\epsilon_0 m_e)^{1/2}$ and $\Omega_e = eB_0/m_e$, the Alfvén speed $v_A = B_0/(\mu_0 n_0 m_i)^{1/2} = c/20$, and the system size is $L_x \times L_z = (25.6d_i)^2$, using 512^2 grids, where 1 grid $= 0.05d_i$. The time step is $0.19\omega_{pe}^{-1}$. The boundary condition is periodic in the x direction and conducting walls in the z direction.

Since results with different guide fields are similar to the results with $B_G = 0.2B_0$ (run 2), in this paper, we will mainly show results with $B_G = 0.2B_0$.

Figures 1(a)–1(h) show color contours of several quantities in run 2 ($B_G = 0.2B_0$) at $\Omega_i t = 38.3$, where Ω_i is the ion cyclotron frequency based on B_0: electron density n_e (a), magnetic field B_y (b), electric fields E_z (c), E_y (d), and E_x (e), and electron fluid velocities V_{ex} (f), V_{ey} (g), and V_{ez} (h). The gray curves on each plot are the projection of magnetic field lines on the x-z plane, where x is the outflow direction and z is the inflow direction. The density n_e is higher in the magnetosheath side, $z < 0$, than in the magnetospheric side, $z > 0$, and shows a little left-right asymmetry due to a small guide field. In the panels from (a) to (d), the right panels next to each contour panel are the one-dimensional (1-D) profiles of each quantity along $x = x_X = -0.3d_i$, which is drawn as the white dashed line in each contour plot passing through the X-line, where the subscript X represents the value at the X-line. The magnetic field B_y varies in x and z, but $\sim 0.2B_0$ across the dashed line, as seen in the 1-D profile of B_y in the right panel. In the 1-D panel, we also plotted the B_x profile, which becomes zero at $z = z_X = 0.05d_i$. In the outflow regions, where $|x| > 0$, B_y changes significantly, but as long as we focus on near the electron stagnation point, located in the magnetospheric side of the EDR around $x = x_X$ and $z = z_X + 0.45d_i$, the B_y strength is of the order of $0.2B_0$. Near the electron stagnation point is the region we will focus on to discuss VDFs in this study.

The Hall electric field E_z exists mainly in the magnetosphere, $z > 0$. It is nonzero and negative at the X-line, at $z = z_X = 0.05d_i$, and $|E_z|$ decreases to zero in the magnetosheath side at $z = z_X - 0.4d_i$. We denote this position as $z = z_c$ as shown in the 1-D profile in the right panel. $|E_z|$ increases as the 1-D panel shows, up to $z = z_X + 0.6d_i$, and then it decreases. There is a clear layer of E_z along the separatrices in the magnetospheric side. The reconnection electric field E_y is positive around $0.1B_0v_A$. The electric field E_x is enhanced mostly

Published under license by AIP Publishing

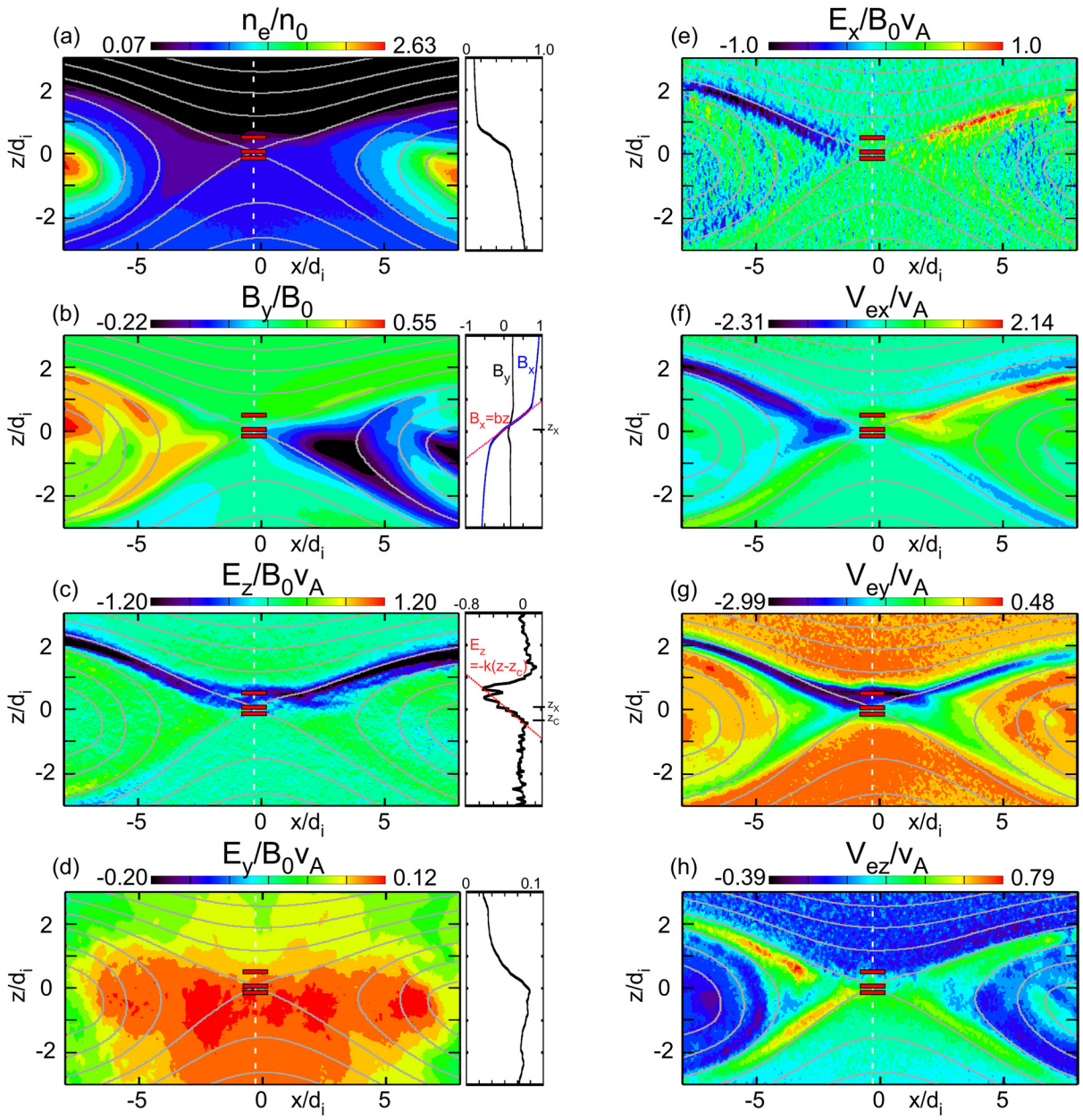

FIG. 1. Contours of electron density n_e (a), out-of-plane magnetic field B_y (b), Hall electric field E_z (c), reconnection electric field E_y (d), electric field E_x (e), electron outflow velocity V_{ex} (f), electron out-of-plane flow V_{ey} (g), electron inflow velocity V_{ez} (h) for run 2 ($B_G = 0.2B_0$) at $\Omega_i t = 38.3$. The gray curves are magnetic field lines. In panels (a)–(d), the right panel shows a 1-D profile of each quantity along the line $x = x_X$ (vertical white dashed line). Density n_e is high in the magnetosheath ($z < 0$). B_y along $x = x_X$ is around $0.2B_0$. Hall electric field E_z is a linearly decreasing function in the magnetosphere ($z > 0$) and the maximum of $|E_z| \sim 0.7B_0v_A$. The reconnection electric field $E_y \sim 0.1B_0v_A$. In the 1-D profile of B_y, the profile of B_x is also shown. The red line $B_x = bz$ in (b) and the red line $E_z = -k(z - z_c)$ in (c) are linear approximations used in this study. In the magnetosphere, at $x = x_X$ and $z = z_X + 0.45d_i$ is the electron stagnation point, where $V_{ez} = 0$ [see panel (h)]. The three red boxes in each panel (top at $z = z_X + 0.45d_i$, middle at $z = z_X$, bottom at $z = z_X - 0.2d_i$) are where electron VDFs in Fig. 2 are measured.

in the region where E_z is negative and large; however, E_x is noisy and small in the vicinity of the X-line.

The electron fluid velocity V_{ex} shows a pair of outflows in the x direction, mostly along the magnetospheric side separatrices. Along those separatrices, there is an enhancement of $|V_{ey}|$, which is responsible to generate a thin current density layer in the reconnection region. The inflow V_{ez} shows a positive value at the X-line, and the stagnation point is located in the magnetospheric side, around $x = x_X$ and $z = z_X + 0.45d_i$.

In panels (a)–(h), the red boxes are where we measure electron VDFs shown in Fig. 2. The center of each box is at $x = x_X = -0.3d_i$,

Published under license by AIP Publishing

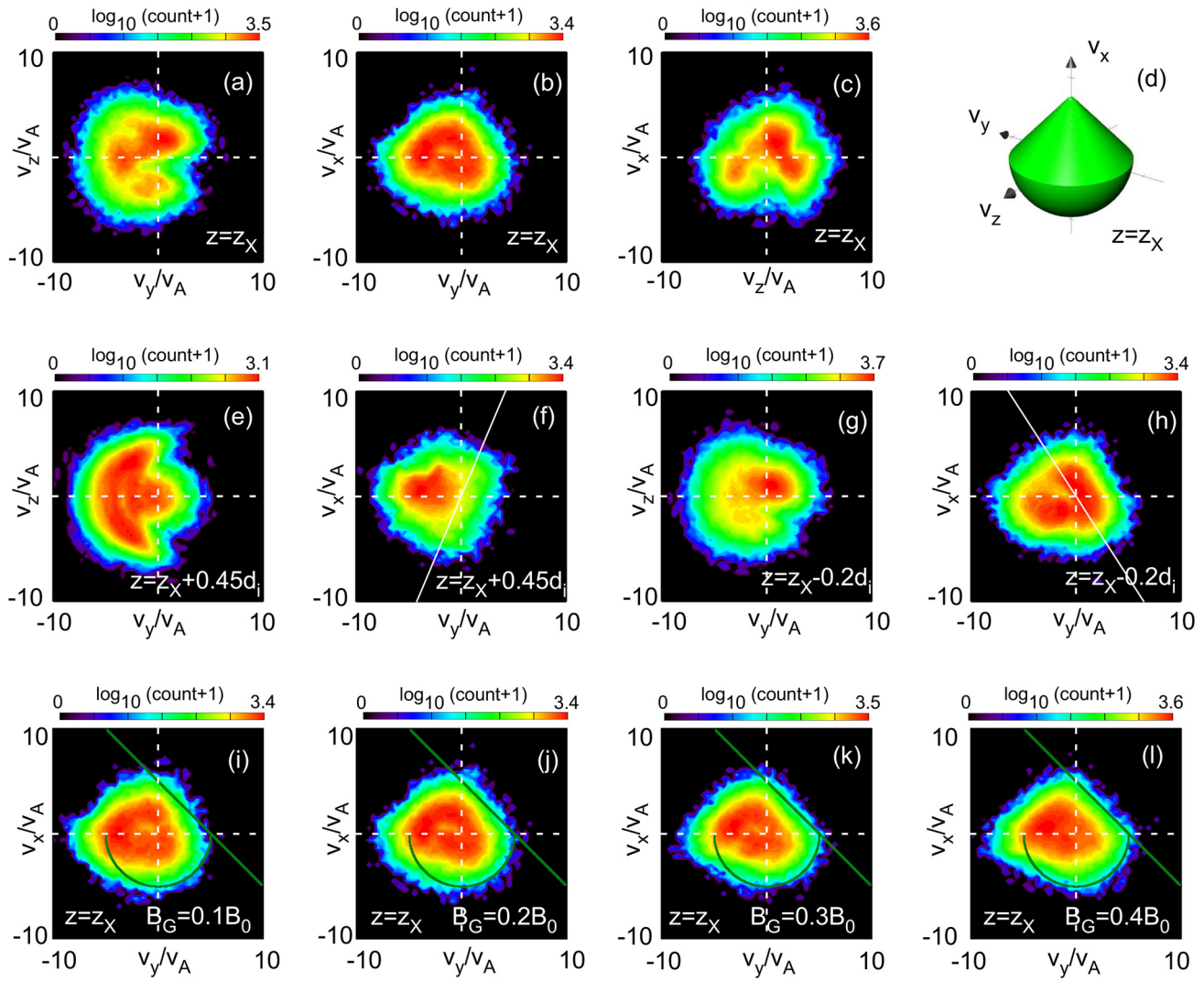

FIG. 2. Top row: (a)-(c) Reduced electron VDFs at the X-line ($x = x_X$ and $z = z_X$). This is modeled as a VDF shape composed of a cone and a hemisphere [panel (d)]. Middle row: (e) and (f) Electron VDF at the electron stagnation point $x = x_X$ and $z = z_X + 0.45d_i$. Panel (e) shows a crescent shape, while panel (f) shows a meandering component and a magnetized component (rectangular shape). The white solid line is parallel to the magnetic field. (g) and (h) Electron VDF at $x = x_X$ and $z = z_X - 0.2d_i$ (magnetosheath). Bottom row: (i)–(l) X-line VDF for each run with the different guide field strength. The green line is $v_x = 5v_A - v_y$, and the green circle is $v_x = -[(5v_A)^2 - v_y^2]^{1/2}$. The X-line VDF looks independent from the guide field strength. Note that VDFs are based on the counts of particles in each bin during 10 time steps in the simulation.

and the box size is $1d_i$ in the x direction and $0.1d_i$ in the z direction. Since the EDR is elongated in the x direction, VDFs around the X-line exhibit a weaker variation in x in the vicinity of the X-line than in the z direction. Therefore, we use a longer x size than the z size of the box to obtain better counting statistics for VDF data. The top red box is at the stagnation point, $z = z_X + 0.45d_i$, the second box is at the X-line, $z = z_X$, and the bottom box is at $z = z_X - 0.2d_i$, in the magnetosheath. Figures 2(a)–2(c) show the electron VDF at the X-line. These are reduced VDFs integrated along the third direction in each plot. Figure 2(a), the v_y-v_z plot, shows a circular structure with an opening near $v_z = 0$ and $v_y > 0$, which is a U-shaped VDF.[6] Figures 2(b) and 2(c) show other velocity planes, v_y-v_x and v_z-v_x, respectively, and the VDF in $v_x > 0$ shows a triangular shape, while the VDF in $v_x < 0$ shows a circular shape. We approximate this VDF at the X-line as a "cone" + a "hemisphere," as shown in diagram (d). In Sec. III, we will consider a mapping of this VDF to a VDF away from the X-line. More details about this approximated VDF in panel (d) will be discussed in Sec. III.

Panels (e)–(h) in Fig. 2 show VDFs in both $z > z_X$ and $z < z_X$ sides. Figures 2(e) and 2(f) are at the stagnation point, $z = z_X + 0.45d_i$, in the magnetosphere, while Figs. 2(g) and 2(h) are at $z = z_X - 0.2d_i$, in the magnetosheath. In the magnetosphere [Figs. 2(e) and 2(f)], the electrons show a crescent in the v_y-v_z plane, and the crescent electrons are energized by E_z^2 as well as the reconnection

Published under license by AIP Publishing

electric field E_y.[6] In the magnetosheath [Figs. 2(g) and 2(h)], crescent electrons also can be seen. In the v_y-v_x velocity plane, in both magnetosphere and magnetosheath sides, shown in panels (f) and (h), there are magnetized rectangular VDFs, elongating in the magnetic field direction, which is along the white solid lines. These magnetized electrons are convected from the upstream, and they have not started meandering motion across the current sheet. These magnetized population can be easily recognized, because their boundaries are parallel to the local magnetic field, which is along the white straight line. On top of each rectangular magnetized electrons, the meandering population is seen, predominantly in $v_x > 0$ in $z > z_X$ in panel (f), and $v_x < 0$ in $z < z_X$ in panel (h).

III. 1-D THEORETICAL MODEL WITH a GUIDE FIELD AND THE DEPENDENCE OF ELECTRON VDFS ON THE *z* POSITION

In this section, discussing electron meandering motion in simplified 1-D fields, we will derive the shape of a crescent VDF in guide field asymmetric reconnection, and we will elucidate the effects of a guide field on electron VDFs. In the theory, the reconnection X-line is set to be at the position $x = 0$ and $z = 0$. We will model a current sheet as a 1-D structure, where all the field quantities depend only on the z position. This 1-D treatment can be applied in the EDR, especially around the line $x = 0$. In our previous study,[6] it is discussed that the applicable range of a 1-D model is, roughly speaking, $-1d_i \leq x \leq 1d_i$ for zero-guide field reconnection. However, as we will discuss in Sec. IV, a guide field introduces left-right asymmetry, in terms of the x position with respect to the X-line, for the shapes of VDFs, even within $\pm 1d_i$ from the X-line. Therefore, in this section, we will focus on VDFs on the line $x = 0$, and later in Sec. IV, we will generalize the theory of VDFs to general x positions. We note that in this section, we only focus on electron VDFs in the magnetospheric side, in $z > 0$, due to meandering electrons, and we do not consider the magnetized electrons coming from the magnetospheric side seen in Fig. 2.

Under this 1-D model, we will discuss two important aspects of a crescent VDF in the v_y-v_z plane. We will focus on only the inner boundary of a crescent, which is the right-side boundary seen in Figs. 3(b)–3(d). One important aspect is the v_y-intercept at $v_z = 0$ of the parabola that describes a crescent shape. Another important aspect is the opening angle of the parabola. Using cuts of a VDF in various v_y-v_z planes for fixed v_x values, we will show that the intercept of the parabola depends on the guide field strength, but the opening angle of the parabola in each cut of a VDF is independent from the guide field. However, we will demonstrate that the opening angle of the parabola in a reduced VDF integrated in the v_x direction does depend on the guide field strength, owing to the superposition effect of each cut of

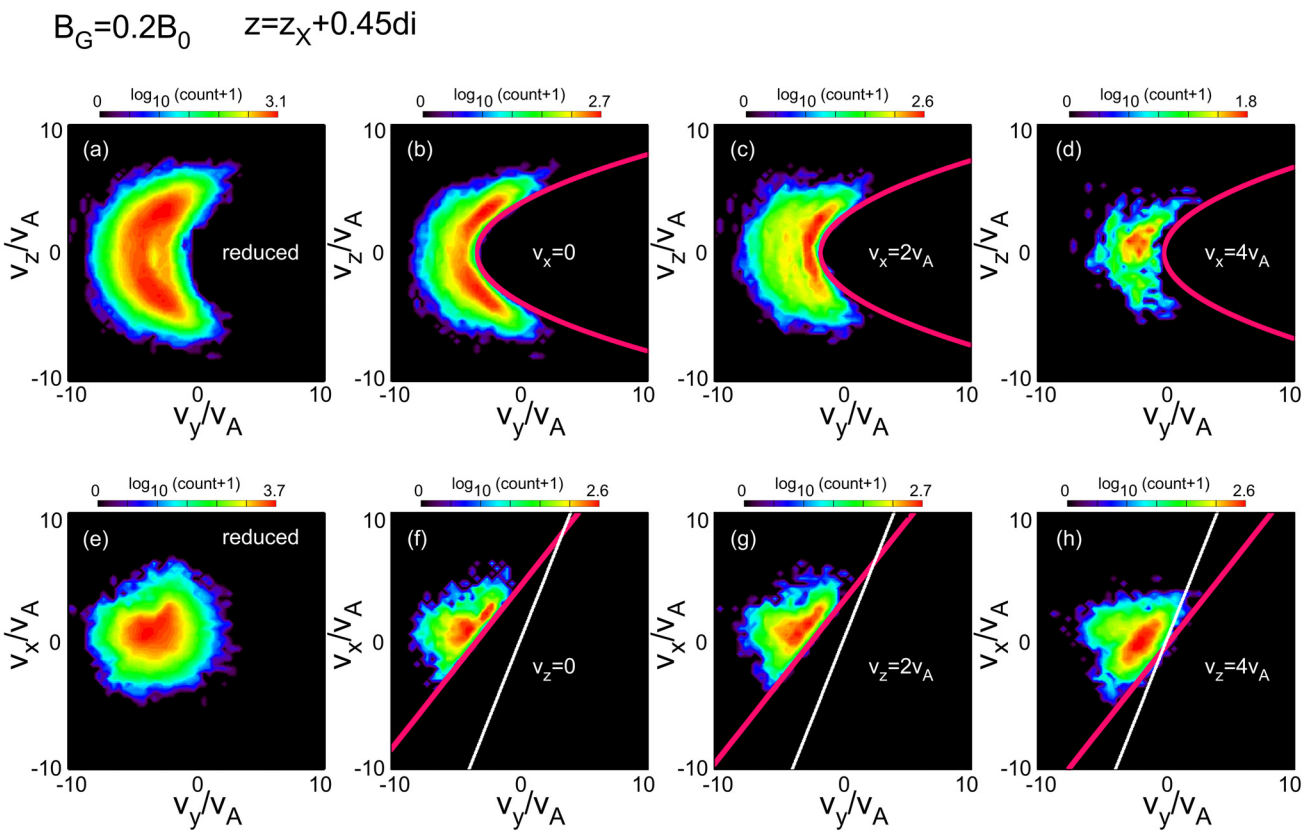

FIG. 3. Cuts of the VDF at $x = x_X$ and $z = z_X + 0.45d_i$ for run 2 ($B_G = 0.2B_0$). (a) Reduced VDF in the v_y-v_z plane. (b)–(d) Cuts of the VDF in various v_x planes. Magenta parabolas are Eq. (5) in various v_x planes. The intercept of the parabola depends on v_x. (e) Reduced VDF in the v_y-v_x plane. (f)–(h) Cuts of the VDF in various v_z plane. Magenta straight lines are Eq. (5) in various v_z planes, and white lines are parallel to the magnetic field. VDFs are elongated along the theoretical lines.

Published under license by AIP Publishing

the VDF. The larger the guide field is, the larger the opening angle of the crescent in the reduced VDF becomes. In the following, we will first discuss cuts of a VDF, and then we will discuss the reduced VDF.

Let us assume a magnetic field $\boldsymbol{B} = (B_x, B_y, B_z) = (bz, B_g, 0)$, and an electric field $\boldsymbol{E} = (E_x, E_y, E_z) = [0, E_r, -k(z - z_c)U(z - z_c)]$, where B_g and E_r are a uniform guide field and a reconnection electric field, respectively. $U(z - z_c)$ is a shifted step function, which is 1 when $z \geq z_c$ and zero when $z < z_c$. This E_z represents the Hall electric field, and simulations show that $z_c < 0$, as seen in the right panel of Fig. 1(c). B_x in all z and $|E_z|$ in $z \geq z_c$ are linearly increasing functions of z, and b and k are constants. Note that the E_z profile for run 2 [$B_G = 0.2B_0$, the right panel of Fig. 1(c)] shows fairly good agreement with the linear profile; however, in run 3 ($B_G = 0.3B_0$) and run 4 ($B_G = 0.4B_0$), actual E_z profiles are not consistent with a linear profile, but there are two peaks in E_z in $z_X < z < z_X + 0.7d_i$ (data not shown). A theory taking into account the E_z variations could be developed, but it is beyond the scope of this paper. Nonetheless, we will apply a linear profile of $E_z = -k(z - z_c)$ to all the simulation runs in this study, by fitting a linear curve to extract the parameter k from simulation data, and the results are shown in Table I.

Focusing on the vicinity of the $x = 0$ line, we neglect B_z and E_x in this analysis. The reconnection electric field E_r is $\sim 0.1B_0v_A$, much smaller than E_z, compared with the maximum of $E_z \sim 0.7B_0v_A$ along the line $x = x_X$. In the analysis below, we discuss the zero-th order motion of electron, neglecting acceleration by $E_y = E_r$, and we set $E_r = 0$. Also, our discussion will be limited to VDFs in the magnetosphere, $z > 0$, where the crescent shape in VDFs becomes outstanding, due to the energization by the Hall electric field E_z.[2,4] We will not consider the magnetized electrons coming from the magnetospheric side; therefore, in the following, VDFs in simulation results after Fig. 3 are composed of only magnetosheath electrons, which come from $z < 0$. There must be small numbers of meandering electrons from the magnetospheric side, too, but the density of the meandering magnetosheath electrons is dominant in VDFs. Thus, in the following, we will show VDFs due to only magnetosheath electrons.

First, we will derive two constants of motion from the momentum conservation law. In $z \geq z_c$, E_z can be eliminated by moving into the reference frame with a drift speed $\boldsymbol{v}_d = (-kz_c/B_g, -k/b, 0)$. In the following, we use a subscript d in variables in this drifting frame, and we have relationship $v_{xd} = v_x + kz_c/B_g$, $v_{yd} = v_y + k/b$, $v_{zd} = v_z$, and $z_d = z$. Let us discuss particle motion in $z \geq z_c$ in the drifting frame, where $E_{zd} = 0$, and no energization occurs. The equation of motion in the drifting frame is $m dv_{xd}/dt = e(dz_d/dt)B_g$, and $m dv_{yd}/dt = -e(dz_d/dt)bz_d$, where m is the electron mass, and integrating these equations, we obtain

TABLE I. Parameters in each simulation run.

Run 1 ($B_g = 0.1B_0$)	$b = 1.26B_0/d_i$, $k = 0.711B_0v_A/d_i$, $B_g = 0.112B_0$, $z_c = -0.326d_i$
Run 2 ($B_g = 0.2B_0$)	$b = 1.10B_0/d_i$, $k = 0.541B_0v_A/d_i$, $B_g = 0.175B_0$, $z_c = -0.407d_i$
Run 3 ($B_g = 0.3B_0$)	$b = 1.08B_0/d_i$, $k = 0.439B_0v_A/d_i$, $B_g = 0.237B_0$, $z_c = -0.503d_i$
Run 4 ($B_g = 0.4B_0$)	$b = 1.20B_0/d_i$, $k = 0.619B_0v_A/d_i$, $B_g = 0.328B_0$, $z_c = -0.395d_i$

$$v_{xd0} = v_{xd} - \frac{eB_g}{m}z_d, \left(\text{or } v_{x0} = v_x - \frac{eB_g}{m}z\right), \tag{1}$$

$$v_{yd0} = v_{yd} + \frac{eb}{2m}z_d^2, \left(\text{or } v_{y0} = v_y + \frac{eb}{2m}z^2\right), \tag{2}$$

where the subscript 0 represents the value at $t = 0$, and we assume that a particle is at $z = z_d = 0$ at $t = 0$. These equations represent the canonical momentum conservation in the x and y directions. In the above Eqs. (1) and (2), the relationship in both drifting and nondrifting frames are shown.

Considering the above two constants of motion based on the initial position at $z = 0$, and combining them with the energy conservation law, let us obtain the region in the velocity space where a VDF of meandering electrons is confined. In this drifting frame, since there is no electric field, the particle's kinetic energy is conserved, and we have

$$v_{xd}^2 + v_{yd}^2 + v_{zd}^2 = v_{xd0}^2 + v_{yd0}^2 + v_{zd0}^2, \tag{3}$$

where the right-hand side represents the constant initial energy at $z_d = z = 0$. Substituting v_{xd0} and v_{yd0} from Eqs. (1) and (2), respectively, into Eq. (3), we obtain

$$v_{yd} = \frac{m}{eb}z_d^{-2}v_{zd}^2 - \frac{1}{4}\frac{eb}{m}z_d^2 + 2\frac{B_g}{bz_d}v_{xd} - \frac{eB_g}{m}\frac{B_g}{b} - \frac{m}{eb}z_d^{-2}v_{zd0}^2. \tag{4}$$

Now we consider the fact that $v_{zd0}^2 \geq 0$, and the particles whose $v_{zd0} = 0$ give the largest v_y-intercept for the above equation. Using this condition $v_{zd0}^2 \geq 0$, and changing the frame from the drifting frame with the subscript d to the nondrifting frame without the subscript d using $v_{xd} = v_x + kz_c/B_g$, $v_{yd} = v_y + k/b$, $v_{zd} = v_z$, and $z_d = z$, we obtain the following inequality:

$$v_y \leq \frac{m}{eb}z^{-2}v_z^2 - \frac{1}{4}\frac{eb}{m}z^2 - \frac{k}{b} + 2\frac{B_g}{bz}\left(v_x + \frac{kz_c}{B_g}\right) - \frac{eB_g}{m}\frac{B_g}{b}. \tag{5}$$

This represents the region in the velocity space where meandering electrons can exist. Note that the sum of the first three terms in the right-hand side gives the same parabola as in reconnection with the zero guide field,[2,6] and the sum of the rest terms with B_g represents the guide field effect, which gives a shift of the intercept. The intercept is a function of v_x, too. Note also that in the above equation, we used the condition $v_{zd0}^2 \geq 0$, but rigorously speaking, that condition can be applied only to $v_{xd0} < 0$ (see the Appendix A); when $v_{xd0} \geq 0$, the condition becomes $v_{zd0}^2 \geq c_z$, where c_z is a function of v_{xd0} and v_{yd0} given by Eq. (A5). However, since c_z is negligibly small under the range of guide field in this study, less than 50% of B_0, Eq. (5) is sufficiently close to the rigorous expression. In this paper, in Subsection III A, using the above inequality Eq. (5), we will discuss cuts of a VDF in various v_x planes and v_z planes.

A. Cuts of a VDF in the v_y-v_z plane and in the v_y-v_x plane

Let us discuss velocity space cuts in the v_y-v_z plane, which are constant-v_x planes. In each cut of a VDF in a constant-v_x plane, the parabola Eq. (5) represents the inner boundary of a crescent VDF based on a specified v_x value. Figures 3(a)–3(d) show the reduced VDF and multiple cuts of the VDF at $x = x_X$ and $z = z_X + 0.45d_i$ in the simulation (run 2, $B_G = 0.2B_0$) for various v_x values, and theoretical

Published under license by AIP Publishing

curves based on Eq. (5). We only used meandering electrons coming from the magnetosheath, $z < 0$. Therefore, although the position of the VDF measurement at $z = z_X + 0.45d_i$ is the same as that in Fig. 2(e), the VDF in Fig. 3(a) is different from Fig. 2(e), and the difference is due to the removed particles, i.e., magnetospheric particles. In each cut based on v_x, the range of the velocity is $\pm 0.5v_A$ from the specified v_x plane. These panels (b)–(d) show that the v_y-intercept of the parabola varies depending on the v_x value, as explained by Eq. (5). To draw these theoretical curves, we used the following parameters measured in run 2 ($B_G = 0.2B_0$) at $\Omega_i t = 38.3$: the slope of B_x is $b = 1.10B_0/d_i$, the slope of E_z is $k = 0.541B_0v_A/d_i$, the guide field $B_g = 0.175B_0$, and the position $z_c = -0.407d_i$. We conclude that the theory, Eq. (5), is in good agreement with the crescent boundary in each v_x-cut of the VDF.

We note that for the z position, since the bin size to measure a VDF is $0.1d_i$ in the z direction, i.e., $z_X + 0.4d_i \le z \le z_X + 0.5d_i$ for this bin to measure the VDF at $z = z_X + 0.45d_i$, we use the z value of the lower boundary of this bin, $z = 0.4d_i$, to draw these theoretical curves, Eq. (5). This is because the smaller the z value is, the narrower the opening angle of the parabola becomes. Note also that the guide field B_g in the actual simulation is not a constant, because the simulation was performed in the system slightly rotated in the x-y plane so that the reconnection rate is maximized,[21] and $B_g = 0.175B_0$ is an average of B_y in the z direction, from $z = z_X - 0.075d_i$ to $z = z_X + 0.625d_i$, along the line $x = x_X$ at $\Omega_i t = 38.3$.

One of the most important guide field effects on meandering electrons in the EDR is manifested as a new structure cut-off in VDFs in a different velocity plane. To see the new cut-off, let us compare various v_z-cuts of the VDF in the v_y-v_x plane. The right-hand side of Eq. (5) gives a linear relationship between v_y and v_x, and the intercept of the linear line on the v_y-axis depends on the v_z value. In Figs. 3(e)–3(h), we plotted the reduced VDF of meandering magnetosheath electrons, which are the same particles as in Fig. 3(a), and multiple cuts of the VDF in various v_z. The theory, drawn as the magenta straight lines, well explains the cut-off of the meandering electrons in the v_y-v_x plane. Here, we again use $z = 0.4d_i$, the lower boundary of the bin, to draw these theoretical curves. Each cut of the VDF shows a structure elongated along the theoretical line.

The slope of the straight line in the v_y-v_x plane in Eq. (5), $v_y \sim 2(B_g/bz)v_x + const.$, shows that the VDF cut-off is not parallel to the magnetic field direction. If it were parallel, the slope would be $v_y \sim (B_g/bz)v_x = (B_y/B_x)v_x$, drawn as the white lines in Figs. 3(f)–3(h). If B_x is a constant, electrons are just gyrating around the magnetic field, and those magnetized particles should appear along the white line. The factor 2 of the slope of the magenta lines results from the fact that electrons are meandering and unmagnetized in $B_x = bz$, which is a linear function of z, i.e., a result of the ratio between the second term in the right-hand side of Eq. (1), $(eB_g/m)z$, and the second term in the right-hand side of Eq. (2), $(eb/2m)z^2$. Equation (5) is

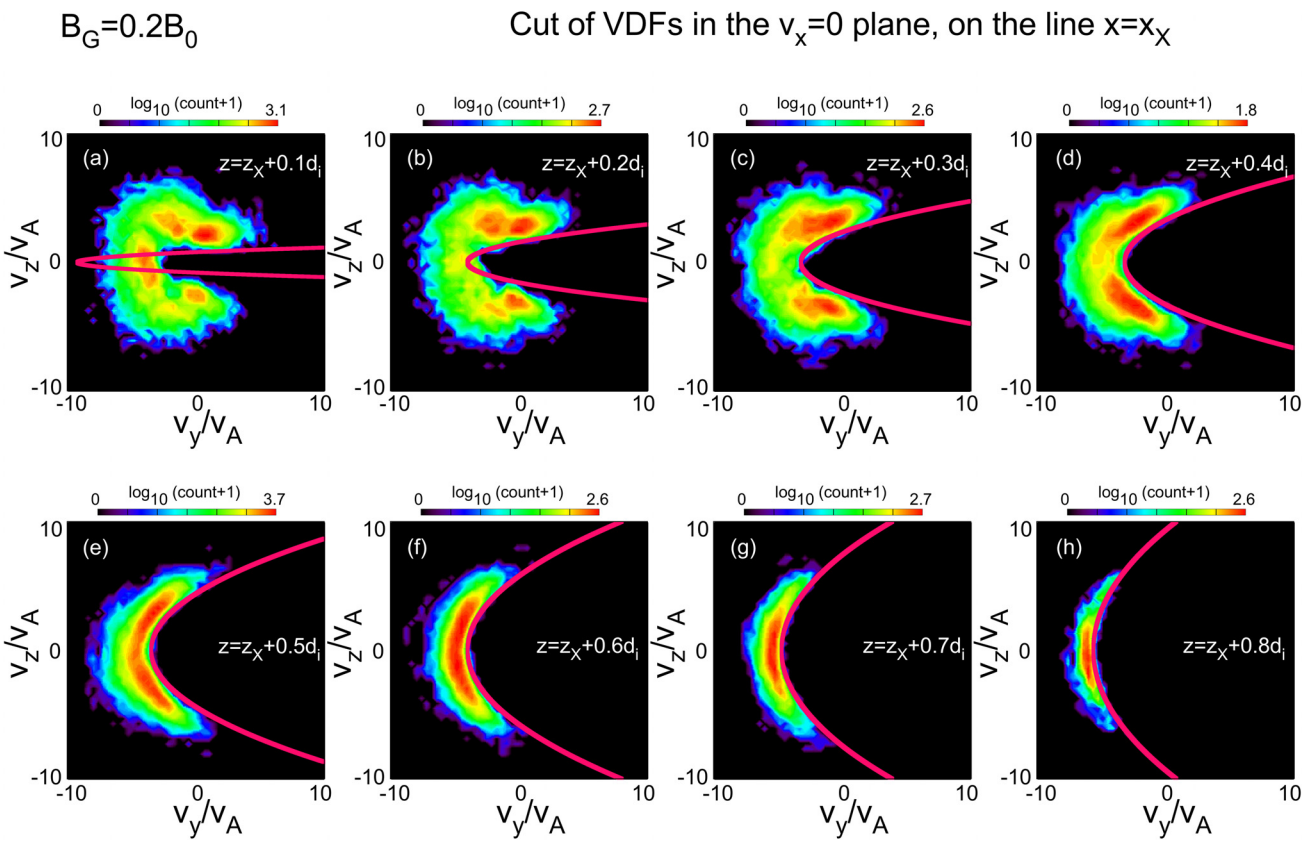

FIG. 4. Dependence of the cut of a VDF at $v_x = 0$ plane on z positions along $x = x_X$ for run 2. Magenta parabolas are Eq. (5) with $v_x = 0$ at various z positions. As we move from a small z to a large z, the opening angle of the parabola becomes wider.

Published under license by AIP Publishing

useful to distinguish crescent electrons due to unmagnetized meandering electrons from the ones due to magnetized electrons, such as discussed by Ref. 22. Note that this discussion is limited only to near $x = 0$; however, in Sec. IV, we will discuss this feature of the nonparallel VDF cut-off in general x positions.

Let us examine the z dependence of crescent electrons. Figure 4 shows crescent electrons in run 2 ($B_G = 0.2B_0$). These are v_x-cuts of VDFs at $v_x = 0$, in the v_y-v_z plane, for the position $x = x_X$ (in the theory, $x = 0$), using only magnetosheath electrons. In each plot, the magenta curve is the prediction of the inner crescent boundary of the VDF, Eq. (5) with $v_x = 0$. As we move from $z = z_X + 0.1d_i$ to $z = z_X + 0.8d_i$, the opening angle of the crescent becomes wider and wider. Except for $z = z_X + 0.1d_i$, the prediction drawn as the magenta curve and the inner boundary of the crescent are in good agreement.

The theoretical curve for $z = z_X + 0.1d_i$ does not match the simulation VDF, as seen in Fig. 4(a), where the v_y-intercept of the theoretical curve is near $v_y = -10v_A$, while the v_y-intercept of the crescent inner boundary of the simulation VDF is near $v_y = -3v_A$. This discrepancy can be attributed to the fact that Eq. (5) does not include the effect of the reconnection electric field E_y. The theoretical curve, Eq. (5), shows that as the value of $z = z_{sp}$, which is a z-position in the magnetosphere, becomes smaller and close to zero, the leftward shift of the curve (v_y-intercept) due to the term $\propto 2B_g/(bz)$ becomes larger. Note that the shift is leftward, since $z_c < 0$. The denominator, bz, in the factor $2B_g/(bz)$ is from the second term in Eq. (2), which becomes zero as $z \to 0$. However, if we include the effect of E_y in the right-hand side of Eq. (2) as a term $-(eE_y/m)t$, where t is the time interval of the motion from $z = 0$ to $z = z_{sp}$, we can avoid this divergence of $2B_g/(bz)$ as $z \to 0$, because the factor becomes $2B_g z/(bz^2 + 2E_y t)$, which does not diverge in the limit $z \to 0$. Therefore, in a more accurate theory that includes E_y, the leftward shift of the theoretical curve would be smaller than in the theoretical curve in Fig. 4(a). Development of such a theory is beyond the scope of this paper.

Figure 5 shows v_z-cuts at $v_z = 0$ of VDFs for run 2, on the line $x = x_X$, from $z = z_X + 0.1d_i$ to $z = z_X + 0.8d_i$. The magenta lines show the theoretical lines based on Eq. (5) for each position of $z = z_{sp}$, using $v_z = 0$. The slope of the line depends on the position $z = z_{sp}$, and the slope in each plot matches the boundary of each VDF cut for positions z larger than or equal to $z_X + 0.3d_i$. For the smaller portions $z = z_X + 0.1d_i$ and $z = z_X + 0.2d_i$, there are many electrons below the theoretical lines. These may be also because we neglected the effect of E_y in the theory, as discussed in Fig. 4. For positions larger than $z = z_X + 0.2d_i$, there is clear agreement between the theoretical predictions and the observed cuts of VDFs.

Figure 6 shows comparisons of v_x-cuts of VDFs at $v_x = 0$ and v_z-cuts of VDFs at $v_z = 0$ for various guide field strengths, from $B_G = 0.1B_0$ to $0.4B_0$, at $z = z_X + 0.5d_i$ and $z = z_X + 0.7d_i$. The parameters of b, k, B_g, and z_c measured in each run are summarized in

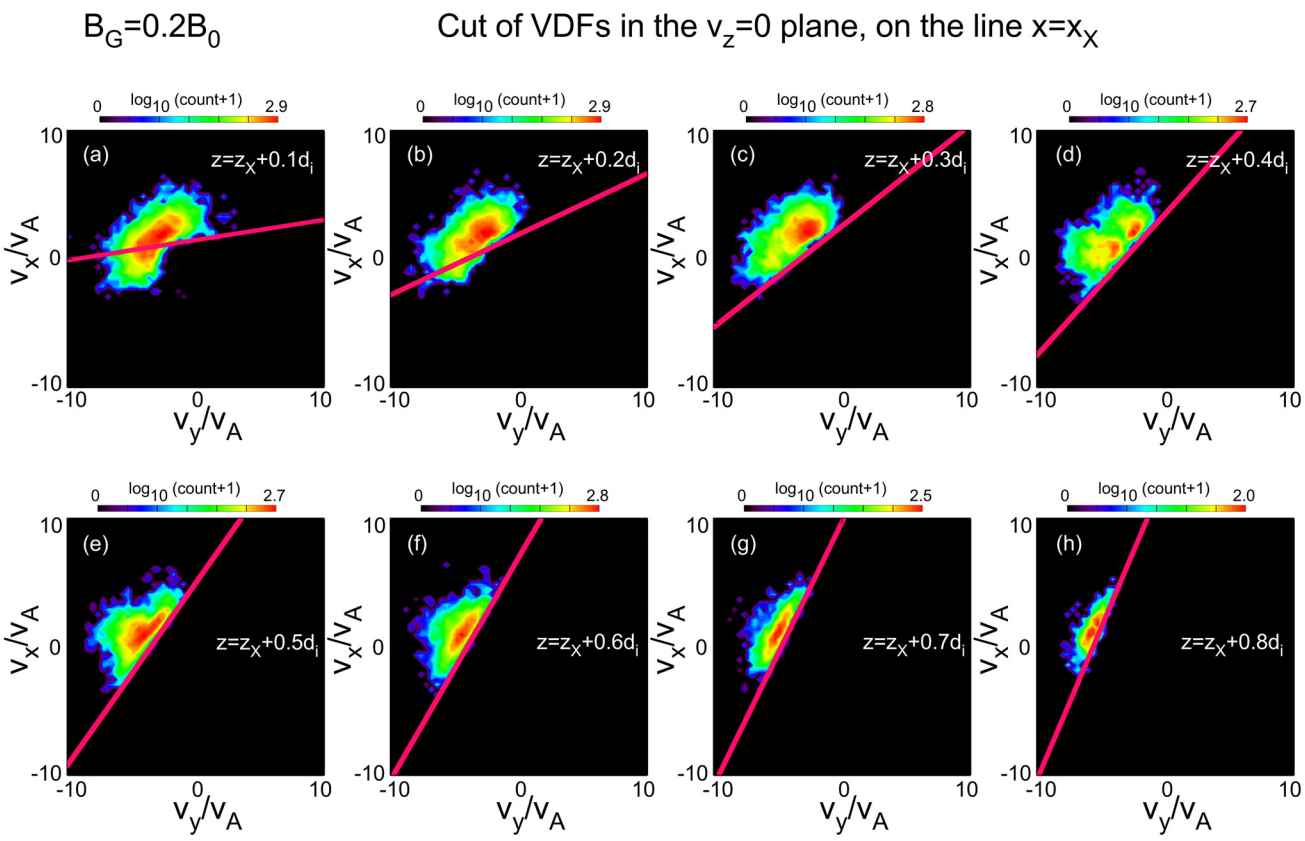

FIG. 5. Dependence of the cut of a VDF at $v_z = 0$ plane on z positions along $x = x_X$ for run 2. Magenta lines are Eq. (5) with $v_z = 0$ at various z positions. As we move from a small z to a large z, the slope of the line changes, and the VDF in each panel is elongated along the theoretical cut-off line.

Published under license by AIP Publishing

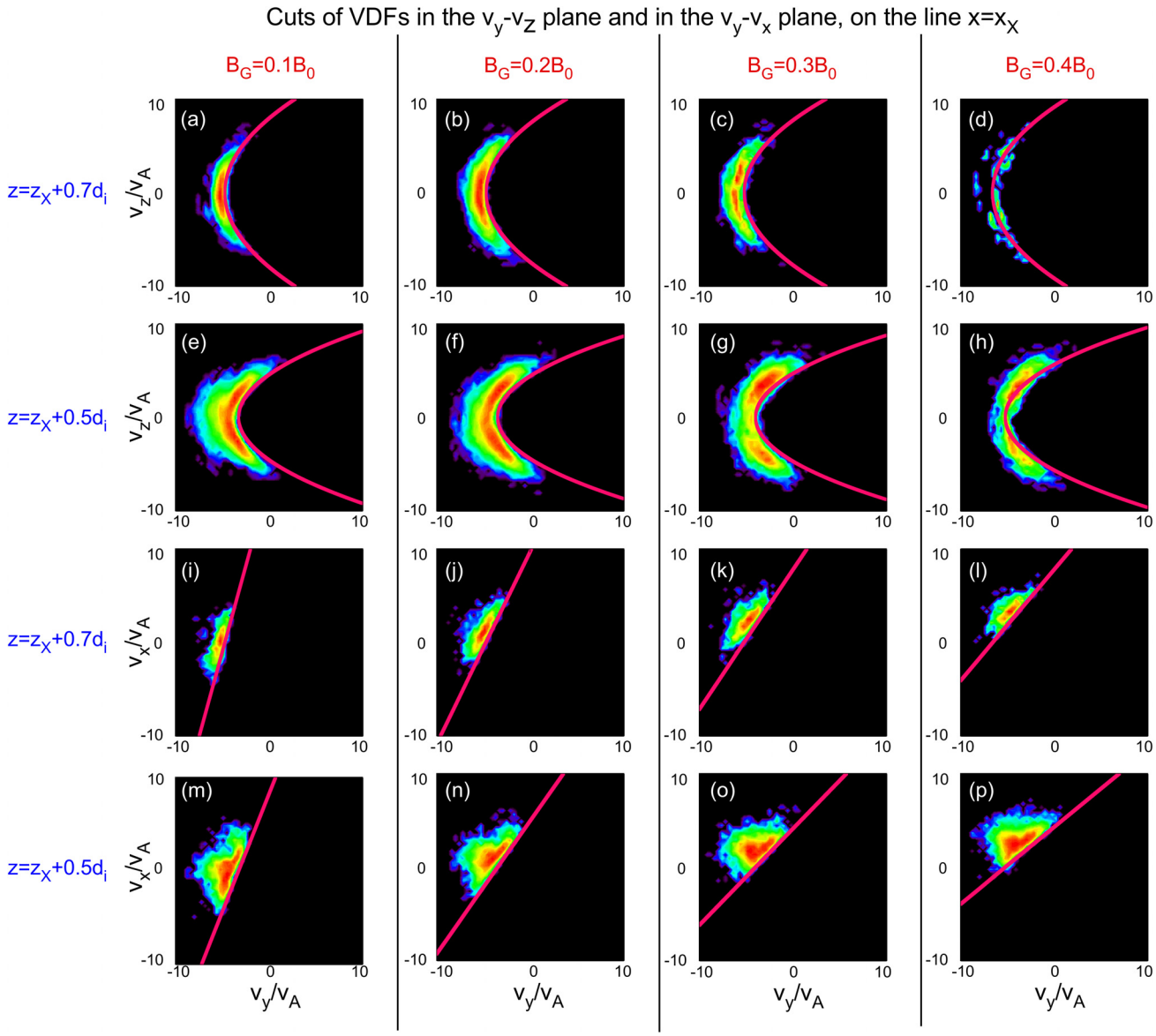

FIG. 6. Dependence of cuts of VDFs on various guide field strength. Top two rows: Cuts of VDFs at $v_x = 0$ at $z = z_X + 0.7d_i$ and $z = z_X + 0.5d_i$. Magenta parabolas are Eq. (5) with $v_x = 0$ in various guide fields. The intercept of the parabola depends on the guide field strength, but the opening angle of the parabola is independent from the guide field. Bottom two rows: Cuts of VDFs at $v_z = 0$. Magenta lines are Eq. (5) with $v_z = 0$ in various guide fields. The slope of the line depends on the guide field, and VDFs are along the theoretical cut-off lines.

Table I. The top two rows [panels (a)–(h)] are v_x-cuts of VDFs in the $v_x = 0$ plane, composed of particles in a velocity range $|v_x| \leq 0.5v_A$. The magenta curves are predictions by Eq. (5) with $v_x = 0$. Depending on the guide field strength, the v_y-intercept of each parabola varies. The intercept is shifted leftward as B_G increases, as predicted by the terms $\propto B_g$ in Eq. (5). The theoretical predictions of the v_y-intercept in Figs. 6(a)–6(d) are: (a) $-4.7v_A$, (b) $-4.7v_A$, (c) $-5.2v_A$, and (d) $-6.6v_A$, and those in Figs. 6(e)–6(h) are (e) $-3.2v_A$, (f) $-3.5v_A$, (g) $-4.0v_A$, and (h) $-5.2v_A$. In contrast, the opening angle of each crescent for the same z position does not strongly vary, and this is expected from Eq. (5), as seen in the first term $(m/eb)z^{-2}v_z^2$, which does not depend on B_g. In simulations, since the slope b is not a fixed constant, as seen in Table I, there is a weak dependence on B_g of the opening angles of crescents; however, those opening angles are almost the same in the same z position, throughout all the guide field strengths. The bottom two rows (panels (i) to (p)) are v_z-cuts of VDFs in the $v_z = 0$ plane, composed of particles in a velocity range $|v_z| \leq 0.5v_A$. Electrons are well explained by Eq. (5) with $v_z = 0$, for all the guide fields, and VDFs show elongated structures along the straight lines. Depending on the guide field strength, the slope of the straight line

Published under license by AIP Publishing

varies. We conclude that cuts of VDFs in constant v_z-planes in the v_y-v_x plane are useful to see the effect of a guide field.

B. Reduced VDF in the v_y-v_z plane

In this subsection, we will discuss the crescent in a reduced VDF in the v_y-v_z plane, and show that the guide field effect can be seen in the reduced VDF more clearly than cuts of VDFs in the v_y-v_z plane. In v_x-cuts of VDFs, Eq. (5) tells that the v_y-intercept of the parabola depends on the guide field, but the opening angle of the parabola does not. However, for the reduced VDF in the v_y-v_z plane, as in Fig. 7(a), the crescent inner boundary does not match the parabola Eq. (5) using a constant v_x. In Fig. 7(a), the two parabolas are based on Eq. (5) using $v_x = 0$ and $v_x = 4v_A$, and the crescent opening angle in the reduced VDF is larger than the openings of those parabolas. This is because, as we will see in this subsection, the projection of the crescent from each layer with different v_x needs to be considered to compose the reduced VDF. The goal of this subsection is to show that the opening angle of the crescent boundary of a reduced VDF depends on the guide field strength, although the opening angle of the parabola in each v_x-cut of the VDF is independent from the guide field.

Let us derive the crescent boundary for a reduced VDF by taking into account this projection effect and considering the mapping between the X-line VDF and a VDF at $z = z_{sp}$ in the magnetosphere. As seen in Figs. 2(a)–2(d), the X-line VDF has a cone in $v_x \geq 0$ and a hemisphere in $v_x < 0$. Figure 7(b) shows this modeled X-line VDF in the v_{y0}-v_{x0} plane, where the subscript 0 represents the initial value at $z = 0$. It shows a triangular structure in $v_{x0} \geq 0$, and the cross section of this cone at a certain v_{x0} is a circle, whose radius takes the maximum at $v_{x0} = 0$. In this model VDF for a guide field $B_G = 0.2B_0$, we assume that the slope of the cone, denoted by s in the following, which is the ratio of the height to the base-radius of the cone, is 1 in $v_{x0} \geq 0$. Simulations show that the slope s is close to 1 for various guide field strengths, in the range $0.1 \leq B_G/B_0 \leq 0.4$. In Figs. 2(i)–2(l), reduced VDFs in the v_y-v_x plane at the X-line, $z = z_X$, in various guide fields from $B_G = 0.1B_0$ to $0.4B_0$ are shown. The green line in each panel represents the line $v_x = -v_y + 5v_A$, and the slope $s = 1$ is in fairly good agreement for every X-line VDF. However, the slope s for a larger guide field case, larger than in this study, $0.4B_0$, can be different from $s = 1$. Keeping this s as a parameter for general strength of B_g, we have

$$v_{x0} = s(v_0 - v_{r0}), \tag{6}$$

where $v_{r0} = (v_{y0}^2 + v_{z0}^2)^{1/2}$ and v_0 represents the radius at $v_{x0} = 0$. In $v_{x0} < 0$, the VDF has a shape different from the cone. In run 1 to run 4, a spherical shape, $v_{x0}^2 + v_{y0}^2 + v_{z0}^2 = v_0^2$, is a good approximation. In Figs. 2(i)–2(l), the green circle in each panel represents the boundary of the sphere $v_{x0}^2 + v_{y0}^2 + v_{z0}^2 = v_0^2$ in $v_x < 0$, and this approximation, neglecting the bulge of the VDFs in the negative v_y direction due to the acceleration by E_y, is in good agreement to explain the lower boundary ($v_{x0} < 0$) of the VDFs in v_y-v_x plane, for guide field $0.1 \leq B_G/B_0 \leq 0.4$. In all the runs, let us use $v_0 = 5v_A$.

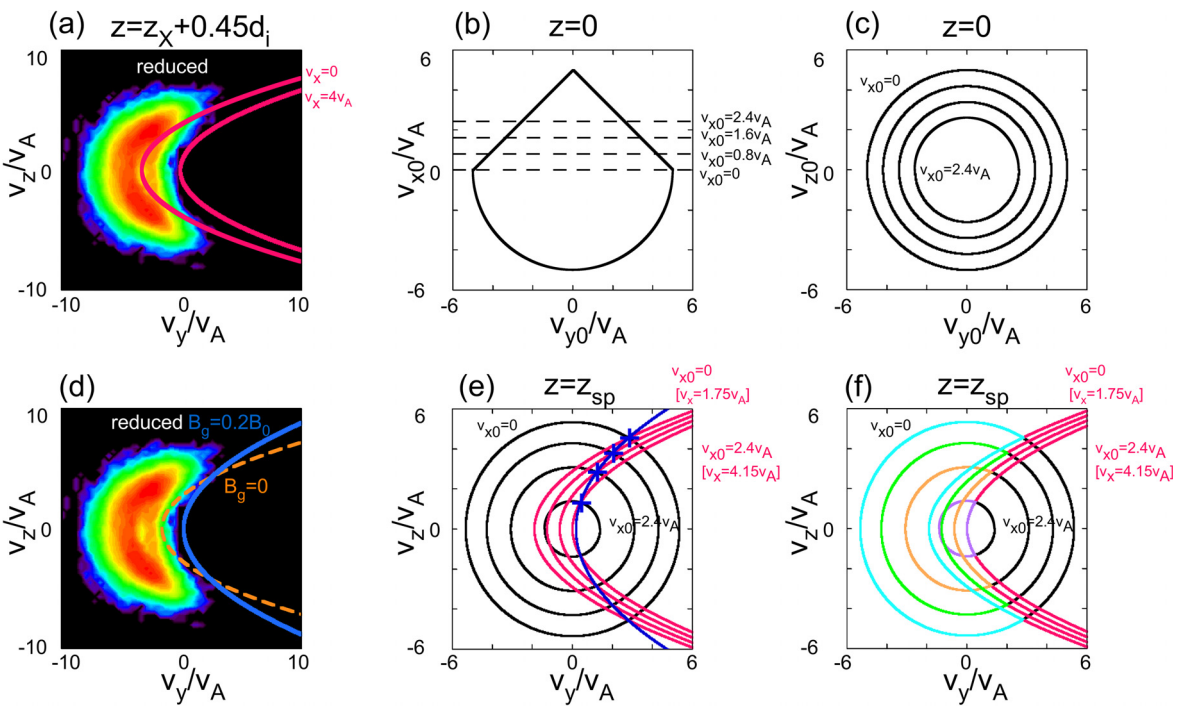

FIG. 7. (a) Reduced VDF in the v_y-v_z plane at $x = x_X$ and $z = z_X + 0.45d_i$ for run 2. The two magenta curves are Eq. (5) with $v_x = 0$ and $v_x = 4v_A$, and the curves do not match the VDF. (b)-(c) Model VDF at the X-line. The X-line VDF in $v_{x0} > 0$ is a cone, and that in $v_{x0} < 0$ is a hemisphere. The four dashed lines are cuts at constant v_{x0} values, and the cross sections are plotted in panel (c). (e)-(f) Mapped circles at $z = z_{sp}$. Each circle is the mapped cross section using Eq. (11). Four magenta parabolas are Eq. (5) using corresponding v_x. Blue crosses are crossing points between the circle and the parabola in each v_x plane. The blue curve is Eq. (17). (f) Region where electrons exist in each v_x layer. (d) Reduced VDF and the theory curve Eq. (17) (blue). The orange dashed curve is the theory curve using $B_g = 0$ and $z_c = 0$.

Published under license by AIP Publishing

In the cone-and-sphere VDF, the slope s in $v_{x0} > 0$ may be related to the slope of the rectangular VDF seen in the magnetosheath. For example, Fig. 2(h), the VDF at $z = z_X - 0.2d_i$, shows a rectangular component due to magnetized electrons, whose slope is determined by the ratio B_x/B_y, the white line in Fig. 2(h). The slope value, B_x/B_y, depends on position z in the magnetosheath, as B_x depends on z, and the slope of the X-line VDF may be determined by the slope of the VDF at the location where electrons in the rectangular VDF start to be unmagnetized, between the position $z = z_X - 0.2d_i$ and $z = z_X$.

We consider the mapping from the cone-and-sphere VDF at the X-line to the VDF at $z = z_{sp}$, a position in the magnetosphere. In Fig. 7(b), four horizontal dashed lines represent examples of four cuts in various v_{x0}. Each cut has a circular cross section with a different radius v_{r0}, determined by Eq. (6). Figure 7(c) shows the cross section circles corresponding to the v_{x0}-cuts in Fig. 7(b). We will consider how the cross section circle in each v_{x0}-layer at $z = 0$ is mapped into the VDF at $z = z_{sp}$, after particle motion from $z = 0$ to $z = z_{sp}$. The electric field $E_z = -k(z - z_c)$ accelerates electrons, and the velocity square $v_x^2 + v_y^2 + v_z^2$ increases. Note that we use variables without subscript 0 to discuss the mapped VDF at $z = z_{sp}$. Considering the energy equation in the nondrifting frame, where E_z accelerates electrons, we obtain the following:

$$v_y^2 + v_z^2 = v_{r0}^2 + v_{x0}^2 - v_x^2 + \phi, \tag{7}$$

where ϕ is the increase in the velocity square due to E_z, obtained by the integral $-2(e/m)\int E_z dz$ from $z = 0$ to $z = z_{sp}$ as

$$\phi = \frac{ek}{m}(z_{sp}^2 - 2z_c z_{sp}). \tag{8}$$

In Eq. (7), the right-hand side includes quantities v_{r0}, v_{x0}, and v_x. If we express v_{r0} and v_{x0} as functions of v_x, the entire right-hand side of Eq. (7) is expressed as a function of v_x, and we can draw the mapped circle $v_y^2 + v_z^2$ for each v_x plane. From Eqs. (1) and (6), we have

$$v_{x0} = v_x - \frac{eB_g}{m} z_{sp}, \tag{9}$$

and

$$v_{r0} = v_0 - s^{-1} v_x + s^{-1} \frac{eB_g}{m} z_{sp}. \tag{10}$$

Substituting these into Eq. (7), we obtain

$$v_y^2 + v_z^2 = s^{-2}\left[v_x - sv_0 - (s^2+1)\frac{eB_g}{m} z_{sp}\right]^2 + \phi - (s^2+1)\left(\frac{eB_g}{m} z_{sp}\right)^2 - 2sv_0 \frac{eB_g}{m} z_{sp}. \tag{11}$$

If we specify a v_x value, the above equation represents a circle in the v_y-v_z plane. Thus, the circle in the v_{y0}-v_{z0} plane with a certain v_{x0} at $z = 0$ is mapped to the circle in the v_y-v_z plane with $v_x = v_{x0} + (eB_g/m)z_{sp}$, which is derived from Eq. (9). Examples of the mapped circles at $z = z_{sp}$ are shown in Fig. 7(e), as four circles with various radii. The largest circle in panel (e) is the mapping from the circle with $v_{x0} = 0$ in panel (c), and smaller circles in panel (e) are mapped from other circles for each v_{x0} in panel (c). The v_x plane corresponding to $v_{x0} = 0$ is $v_x = 1.75v_A$, and the plane corresponding to $v_{x0} = 2.4v_A$ is $v_x = 4.15v_A$, according to Eq. (9) and using the position $z_{sp} = 0.4d_i$ (the lower z boundary of the bin to measure this VDF in Fig. 7) and run 2 parameters in Table I. In this panel (e), we also plotted multiple parabolas based on Eq. (5), using the corresponding four v_x values. The leftmost magenta curve is the parabola for $v_x = 1.75v_A$, corresponding to $v_{x0} = 0$, and the rightmost is for $v_x = 4.15v_A$, corresponding to $v_{x0} = 2.4v_A$.

Now, we are ready to discuss the inner boundary of the reduced VDF in the v_y-v_z plane, by superposing each layer of a constant v_x plane. Each v_x layer has the parabolic boundary of Eq. (5) and the circle of Eq. (11), and both curves depend on the v_x value. As v_x increases, the circle becomes smaller, and the parabola shifts rightward. In each v_x plane, particles must be within the circle and to the left of the parabola. For example, in the plane of $v_x = 1.75v_A$, which corresponds to $v_{x0} = 0$, the particles in that velocity plane must be within the light-blue crescent in panel (f). In the same way, as v_x increases, particles must be within the light green crescent for $v_x = 2.55v_A$, the orange crescent for $v_x = 3.35v_A$, and the purple crescent for $v_x = 4.15v_A$. As shown in panel (f), the parabolic boundary in each crescent from light blue to purple is gradually shifted rightward as v_x increases, and the entire region is the superposition of these different crescents. We compose the inner boundary of the crescent in the reduced VDF by connecting the crossing point of the parabola and the circle in each v_x layer, as seen in blue crossing points in Fig. 7(e).

Solving the system of equations of the circle Eq. (11) and the parabola Eq. (5), we can obtain those crossing points. Each blue cross in $v_z > 0$ in panel (e) shows the crossing point of the circle and the parabola in each v_x-plane. Connecting the crossing points in multiple v_x-layers gives the inner boundary of the crescent in the reduced VDF. In other words, if we eliminate v_x from the system of equations of the circle Eq. (11) and the parabola Eq. (5), we obtain a single equation with variables of v_y and v_z, which represents the inner boundary of the crescent VDF. The opening angle of the blue curve for the crescent in the reduced VDF in panel (e) is larger than that of each magenta curve, which is the crescent in each v_x-layer.

To obtain the analytical expression of the crescent in the reduced VDF, i.e., v_y as a function of v_z, we combine the parabola Eq. (5) and the circle Eq. (11) to eliminate v_x from those system of equations. From Eq. (11), we obtain

$$v_x = sv_0 + (s^2+1)\frac{eB_g}{m} z_{sp} - s\left[v_y^2 + v_z^2 - \phi + (s^2+1)\left(\frac{eB_g}{m}\right)^2 z_{sp}^2 + 2sv_0 \frac{eB_g}{m} z_{sp}\right]^{1/2}, \tag{12}$$

where the minus sign before the brackets in the right-hand side is because the right-hand side of Eq. (10) needs to be positive, i.e., $v_{r0} > 0$. Substituting this v_x into Eq. (5), changing the inequality to the equality and using $z = z_{sp}$, we obtain the following quadratic equation for v_y

$$A_0 v_y^2 + 2A_1 v_y + A_1^2 - A_2 = 0, \tag{13}$$

where A_0, A_1, and A_2 are

$$A_0 = \left[1 - 4s^2\left(\frac{B_g}{bz}\right)^2\right], \tag{14}$$

Published under license by AIP Publishing

$$A_1 = -\frac{m}{eb} z_{sp}^{-2} v_z^2 + \frac{1}{4}\frac{eb}{m} z_{sp}^2 - 2s\frac{B_g}{bz_{sp}} v_0 - (2s^2+1)\frac{eB_g}{m}\frac{B_g}{b} - 2\frac{k}{b}\frac{z_c}{z_{sp}} + \frac{k}{b}, \tag{15}$$

$$A_2 = 4s^2\left(\frac{B_g}{bz_{sp}}\right)^2\left[2s\frac{eB_g}{m} z_{sp} v_0 + (s^2+1)\left(\frac{eB_g}{m}\right)^2 z_{sp}^2 - \phi + v_z^2\right]. \tag{16}$$

Therefore, the inner boundary of the crescent in the reduced VDF is given as

$$v_y = -\frac{A_1}{A_0} - \frac{\left[A_1^2 - A_0(A_1^2 - A_2)\right]^{1/2}}{A_0}. \tag{17}$$

The right-hand side of this equation represents a function of v_z. Although the first term in the right-hand side, $-A_1/A_0$, is written in the form of a parabola, the entire theoretical curve is not a parabola, because the second term in the right-hand side includes A_1 and A_2, both of which are functions of v_z. The crescent curve in a reduced VDF, represented by Eq. (17), depends on the guide field B_g.

In Fig. 7(d), the blue curve shows the theoretical curve Eq. (17). The theory well explains the crescent boundary, and the opening angle of the crescent is larger than the prediction for zero-guide field reconnection, which is drawn as the orange dashed line, obtained by taking $B_g \to 0$ and $z_c \to 0$ in Eq. (17). Note that in the limit of $B_g \to 0$, we recover the same parabola as in the zero-guide-field reconnection:[2] $v_y = -A_1 = (m/eb)z_{sp}^{-2}v_z^2 - (eb/4m)z_{sp}^2 - k/b$, because $A_0 \to 1$, $A_2 \to 0$, and $z_c \to 0$.

The above derivation for the VDF at $x=0$ and $z = z_{sp}$ is based on a 1-D assumption, in which fields are independent from the x position, and electrons are coming to $z = z_{sp}$ from both positive x and negative x regions, with both positive v_x and negative v_x values. However, the crescent boundary is determined by only the positive v_x particles, as discussed in the above, because the shift of the parabola in each v_x-layer is rightward as $v_x(>0)$ increases, as seen in Fig. 7(e). In Sec. IV A, we discuss reduced VDFs in general x positions, but this treatment, considering electrons with $v_x > 0$, is valid only in $x \geq 0$, and, the crescent shape in reduced VDFs in $x<0$ becomes different from Eq. (17).

Figure 8 compares reduced VDFs in the v_y-v_z plane on the line $x = x_X$ for various guide fields from $B_G = 0.1B_0$ (run 1) to $0.4B_0$ (run 4). As we move from $z = z_X + 0.1d_i$ to $z = z_X + 0.7d_i$, the opening angle of the theoretical parabolalike curve becomes wider. Also, there is a tendency that the opening angle of the parabolalike curve widens as the guide field increases, if we compare VDFs at the same z position, from the left panel to the right panel. Those two tendencies, z dependence and B_g dependence, are consistent with the theory Eq. (17). The theoretical curves for $z = z_X + 0.5d_i$ and $z = z_X + 0.7d_i$ match the inner boundary of the reduced VDFs in all the guide fields. At $z = z_X + 0.3d_i$, the theory and the simulations agree except for the region near $v_z = 0$. There is a relatively large gap between the magenta curve and the crescent inner boundary near $v_z = 0$. This can be attributed to the effect of E_y, acceleration of electrons to more negative v_y, which is omitted in deriving Eq. (17). The E_y-effect becomes the most significant in the VDFs at $z = z_X + 0.1d_i$. The lack of particles in the negative v_z region near the center of the crescent, i.e., a large gap between the magenta curve and the negative v_z side of the VDF boundary, in each plot is discussed in our previous study[6] as a U-shaped VDF near the X-line.

C. Reduced VDF in the v_y-v_x plane

Let us discuss the reduced VDF in the v_y-v_x plane, at $z = z_{sp} > 0$. As seen in Figs. 3(f)–3(h), each v_z-cut shows a linear cut-off predicted by Eq. (5), whose direction is nonparallel to the magnetic field. However, the projection of each v_z-cut on the v_y-v_x plane gives a different shape of the reduced VDF boundary as seen in Fig. 3(e). We will show that the guide-field effect on the reduced VDF in the v_y-v_x plane can be understood based on the translational mapping from the X-line VDF.

The VDF mapping from $z=0$ to $z = z_{sp}$ is a simple translational shift, $v_{x0} \to v_x = v_{x0} + (eB_g/m)z_{sp}$ and $v_{y0} \to v_y = v_{y0} - (eb/2m)z_{sp}^2$, based on Eqs. (1) and (2), which are two constants of motion due to the canonical momentum conservation. Figures 9(a) and 9(b) show the reduced VDFs of meandering electrons at the X-line, $z = z_X$, and at $z = z_X + 0.45d_i$, respectively. The translational mapping is seen in the bottom (green) and the right (pink) boundaries because the v_x-shift is in the positive direction, and the v_y-shift is in the negative direction. To draw the theoretical curves, we used $v_{x0} = 5v_A - v_{y0}$, as seen in the pink curve based on Eq. (6) only in the region $v_x \geq 0$, and $v_{x0} = -[(5v_0)^2 - v_{y0}^2]^{1/2}$, as in the green curve in panel (a), and we used $z_{sp} = 0.45d_i$ to compute the translational shifts in v_x and v_y directions, $(eB_g/m)z_{sp}$ and $-(eb/2m)z_{sp}^2$, respectively, for panel (b). The pink and green thick curves are the theoretical curves using the translational shift denoted by the white arrows from the theoretical curves in panel (a). The dashed curves in panel (b) are the same theoretical curves in panel (a).

The direction of the VDF translation is perpendicular to the linear VDF cut-off in each v_z-plane cut, discussed in Sec. III A, and in Figs. 3, 5, and 6. The velocity translation vector, which is denoted as $\boldsymbol{v}_t$, based on Eqs. (1) and (2) is $\boldsymbol{v}_t = [(eB_g/m)z_{sp}, -(eb/2m)z_{sp}^2]$. Since Eq. (5) shows that $v_y \sim (2B_g/bz_{sp})v_x$, the direction of the boundary line of the VDF in each v_z-cut denoted as $\boldsymbol{v}_b$ is $\boldsymbol{v}_b = [1, 2(B_g/bz_{sp})]$. Thus, $\boldsymbol{v}_t \cdot \boldsymbol{v}_b = 0$, and the translational direction of the mapping is perpendicular to the boundary line of VDF cuts.

The left and top boundaries of the reduced VDF at $z = z_{sp} > 0$ are determined by the accessibility of X-line particles. We need to first determine the left and top boundaries of the domain in the X-line VDF for particles that can reach $z = z_{sp}$ from $z=0$. Whether X-line electrons can reach $z = z_{sp}$ is constrained by the energy conservation. The required condition for particles at $z=0$ to reach $z = z_{sp}$ is that the particles at $z=0$ have enough energy so that $v_z^2 \geq 0$ at $z = z_{sp}$. From Eq. (7), we have the condition

$$v_z^2 = v_{r0}^2 + v_{x0}^2 - v_x^2 + \phi - v_y^2 \geq 0, \tag{18}$$

which gives the region in the v_{y0}-v_{x0} plane for particles at the X-line, $z=0$. Another condition for the X-line electrons is that they are confined in the following velocity space:

$$v_{r0}^2 \leq (s^{-1}v_{x0} - v_0)^2 \quad (\text{for } v_{x0} \geq 0), \tag{19}$$

$$v_{x0} \geq -(v_0^2 - v_{r0}^2)^{1/2} \quad (\text{for } v_{x0} < 0), \tag{20}$$

where Eq. (19) represents the inside of the cone in $v_{x0} \geq 0$, and Eq. (20) represents the inside of the hemisphere in $v_{x0} < 0$.

Published under license by AIP Publishing

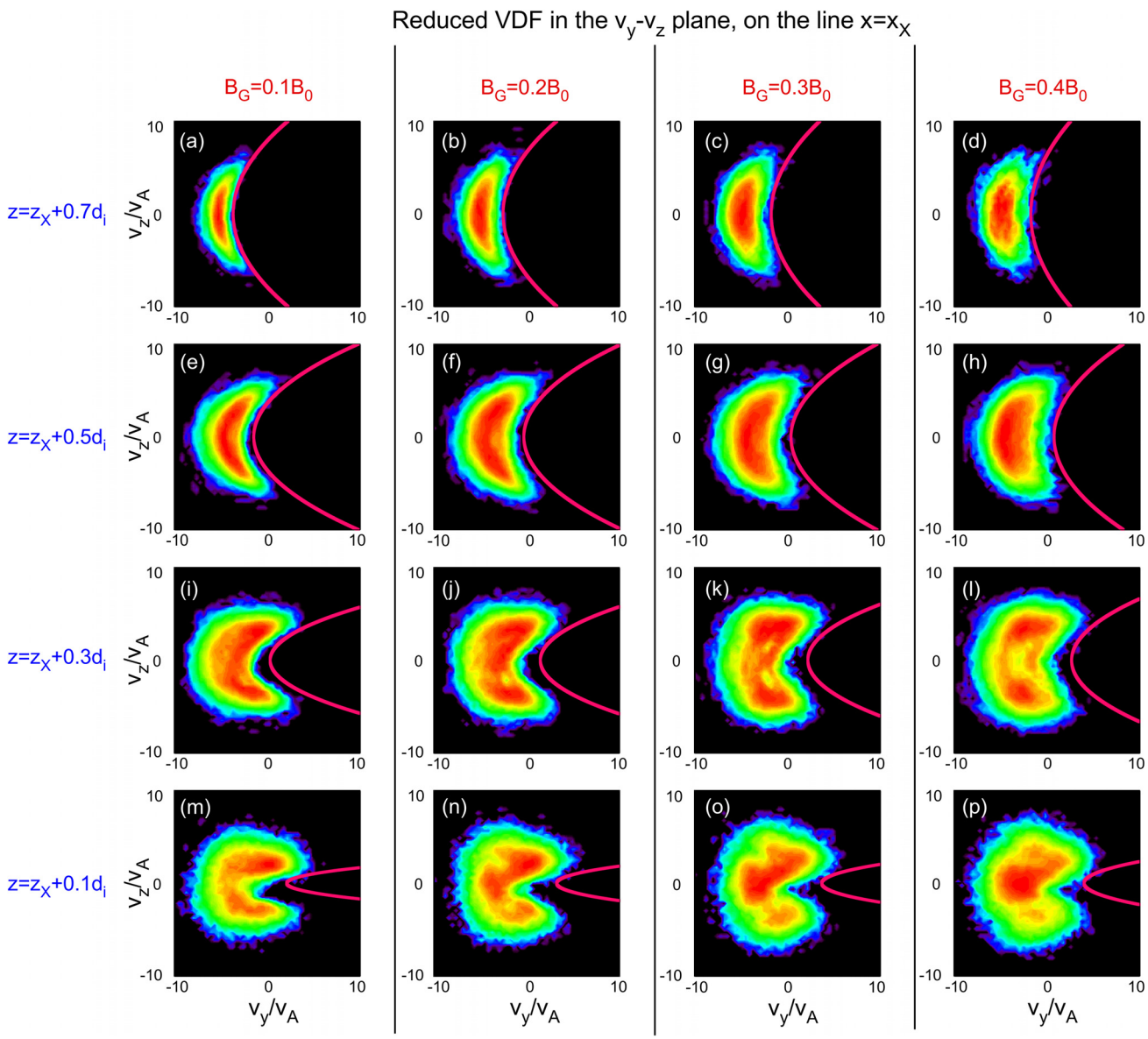

FIG. 8. Dependence of reduced VDFs in the v_y-v_z plane on z positions and various guide field strength ($0.1B_0$ to $0.4B_0$). Magenta parabolas are Eq. (17). The opening angle of the parabola depends on guide field strength, and the opening angle becomes wider as B_G increases.

We combine the above conditions to discuss the particles at $z=0$ that reach $z=z_{sp}$. First, we consider particles with $v_{x0} \geq 0$ in Eq. (19). Substituting v_x and v_y from Eqs. (1) and (2) into Eq. (18), and considering Eq. (19), the inequality Eq. (18) becomes the following:

$$\left(s^{-1}v_{x0} - v_0 - s\frac{eB_g}{m}z_{sp}\right)^2 - \left(v_{y0} - \frac{eb}{2m}z_{sp}^2\right)^2 \geq 2sv_0\frac{eB_g}{m}z_{sp} + (s^2+1)\left(\frac{eB_g}{m}\right)^2 z_{sp}^2 - \phi. \quad (21)$$

This represents a hyperbola for the X-line VDF. In addition, in the v_{y0}-v_{x0} plane, particles are bounded by the cone Eq. (19), equivalent to the following inequalities for v_{x0} and v_{y0}:

$$v_{x0} - sv_0 \leq sv_{y0} \leq -v_{x0} + sv_0. \quad (22)$$

Therefore, in the reduced X-line VDF for $v_{x0} \geq 0$, the particles below these curves, Eqs. (21) and (22), can reach $z=z_{sp}$. See the magenta curve in Fig. 9(c) for Eq. (21), and the pink curve for Eq. (22), and particles surrounded by these and $v_{x0} \geq 0$ can reach $z=z_{sp} = z_X + 0.45d_i$. The particles whose v_{x0} and v_{y0} do not satisfy the above inequalities, Eqs. (21) and (22), will turn back in the z direction before reaching $z=z_{sp}$.

Next, for the X-line electrons with $v_{x0} < 0$, we can determine the boundaries of particles that can reach $z=z_{sp}$ in the same way, considering the energy conservation Eq. (18) and the region Eq. (20). From

Published under license by AIP Publishing

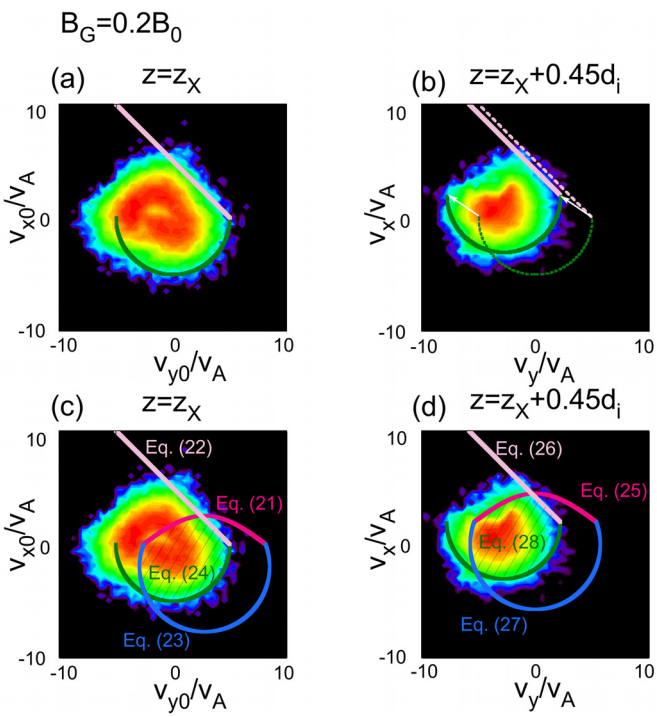

FIG. 9. Reduced VDFs in the v_y-v_x plane for run 2. (a)(c) VDF at the X-line. (b)(d) VDF at $x = x_X$ and $z = z_X + 0.45d_i$. Four curves (magenta, pink, blue, and green) are Eqs. (21)–(24), respectively, in panel (c), and Eqs. (25)–(28), respectively, in panel (d). The shaded area shows a translational mapping.

Eq. (20), we have $v_{r0}^2 + v_{x0}^2 \le v_0^2$, and substituting this into Eq. (18) and using Eqs. (1) and (2), we have

$$\left(v_{x0} + \frac{eB_g}{m} z_{sp}\right)^2 + \left(v_{y0} - \frac{eb}{2m} z_{sp}^2\right)^2 \le v_0^2 + \phi. \tag{23}$$

In addition, from Eq. (20) itself, we have

$$v_{x0} \ge -(v_0^2 - v_{y0}^2)^{1/2}. \tag{24}$$

Therefore, particles of $v_{x0} < 0$ in the X-line VDF within these two boundaries, Eqs. (23) and (24), can reach $z = z_{sp}$. See the green curve for Eq. (24) and the blue curve for Eq. (23) in Fig. 9(c).

Now we have the four boundary curves, Eqs. (21), (22), (23), and (24), corresponding to magenta, pink, blue, and green curves in Fig. 9(c), respectively, to discuss the VDF at the X-line, and the shaded region in Fig. 9(c) surrounded by those four curves represents the particles that can reach the position $z = z_X + 0.45d_i$.

Let us then obtain the corresponding four boundaries at the mapped position $z = z_{sp}$. Again, we will first obtain the mapped boundaries at $z = z_{sp}$ due to particles for $v_{x0} \ge 0$ at $z = 0$. From Eqs. (21) and (22), we can obtain the boundaries of the VDF at $z = z_{sp}$ by translating v_{x0} and v_{y0} to v_x and v_y, respectively, using Eqs. (1) and (2):

$$\left[s^{-1}v_x - v_0 - s^{-1}(s^2+1)\frac{eB_g}{m} z_{sp}\right]^2 - v_y^2 \ge 2sv_0 \frac{eB_g}{m} z_{sp} + (s^2+1)\left(\frac{eB_g}{m}\right)^2 z_{sp}^2 - \phi. \tag{25}$$

$$v_x - sv_0 - \frac{eB_g}{m} z_{sp} - s\frac{eb}{2m} z_{sp}^2 \le sv_y \le -v_x + sv_0 + \frac{eB_g}{m} z_{sp} - s\frac{eb}{2m} z_{sp}^2. \tag{26}$$

Since we limit $v_{x0} \ge 0$ for the above derivation, Eqs. (25) and (26) apply to only the region $v_x \ge (eB_g/m)z_{sp}$, as seen in Eq. (1).

Finally, let us obtain the mapped boundaries at $z = z_{sp}$ due to particles for $v_{x0} < 0$ at $z = 0$. From Eqs. (23) and (24), we obtain the boundaries of the VDF at $z = z_{sp}$ by translating v_{x0} and v_{y0} to v_x and v_y, respectively, using Eqs. (1) and (2)

$$v_x^2 + v_y^2 \le v_0^2 + \phi, \tag{27}$$

$$v_x \ge -\left[v_0^2 - \left(v_y + \frac{eb}{2m} z_{sp}^2\right)^2\right]^{1/2} + \frac{eB_g}{m} z_{sp}. \tag{28}$$

These are obtained from the condition that $v_{x0} < 0$, i.e., $v_x < (eB_g/m)z_{sp}$, as seen in Eq. (1).

For the VDF at $z = z_{sp}$, we have the four boundary curves, Eqs. (25)–(28), corresponding to magenta, pink, blue, and green curves in Fig. 9(d), respectively, and the shaded region surrounded by those four curves in Fig. 9(d) describes the region of the velocity space at $z = z_X + 0.45d_i$ mapped from the X-line VDF.

Comparing Figs. 9(c) and 9(d), we can see the translational mapping between $z = z_X$ and $z = z_X + 0.45d_i$. Note that in Fig. 9(d), there are particles outside the boundaries by Eqs. (27) and (28), left to the blue curve in $v_y < 0$. These particles exist, because of acceleration by the reconnection electric field E_y, which we neglected in this analysis.

As seen in the theory and simulation results, the guide-field effect is the translational shift of electron motion in the v_x direction, and this shift in the v_x positive direction results from electron gyration in a positive guide field B_y. When electrons are moving from $z = 0$ to $z = z_{sp} > 0$, there is a conversion of velocity from a positive v_z to a positive v_x during the gyration. Therefore, for the positive z region in the magnetospheric side, the translational shift in v_x is always positive. In contrast, the transnational shift in the v_y direction is due to particle motion in the magnetic field B_x. Since v_z (>0) is converted to negative v_y during the electron meandering motion in $z > 0$, the shift of v_y always occurs in the negative direction.

Figure 10 shows reduced VDFs in the v_y-v_x plane on the line $x = x_X$ for various z positions and guide fields. In each panel, the magenta, pink, blue, and green curves show the prediction curves based on Eqs. (25)–(28), respectively. The theory predicts that particles surrounded by those four curves are mapped from the corresponding part of the VDF at $z = z_X$ (in the theory, $z = 0$), due to the translational mapping. In VDFs at $z = z_X + 0.7d_i$, most of the particles in each plot are confined in the region surrounded by the four theoretical curves. In VDFs at $z = z_X + 0.5d_i$, there are some electrons outside the region surrounded by the four theoretical curves, in particular, in the left side of the blue theoretical curve. These are particles considered to be accelerated by the reconnection electric field E_y. In the smaller z positions, $z = z_X + 0.3d_i$ and $z = z_X + 0.1d_i$, there are many electrons outside the blue curve and the magenta curve. They tend to be shifted to the negative v_y side, which is also due to the effect of the acceleration by E_y. Overall, the theory and simulations are in good agreement.

Published under license by AIP Publishing

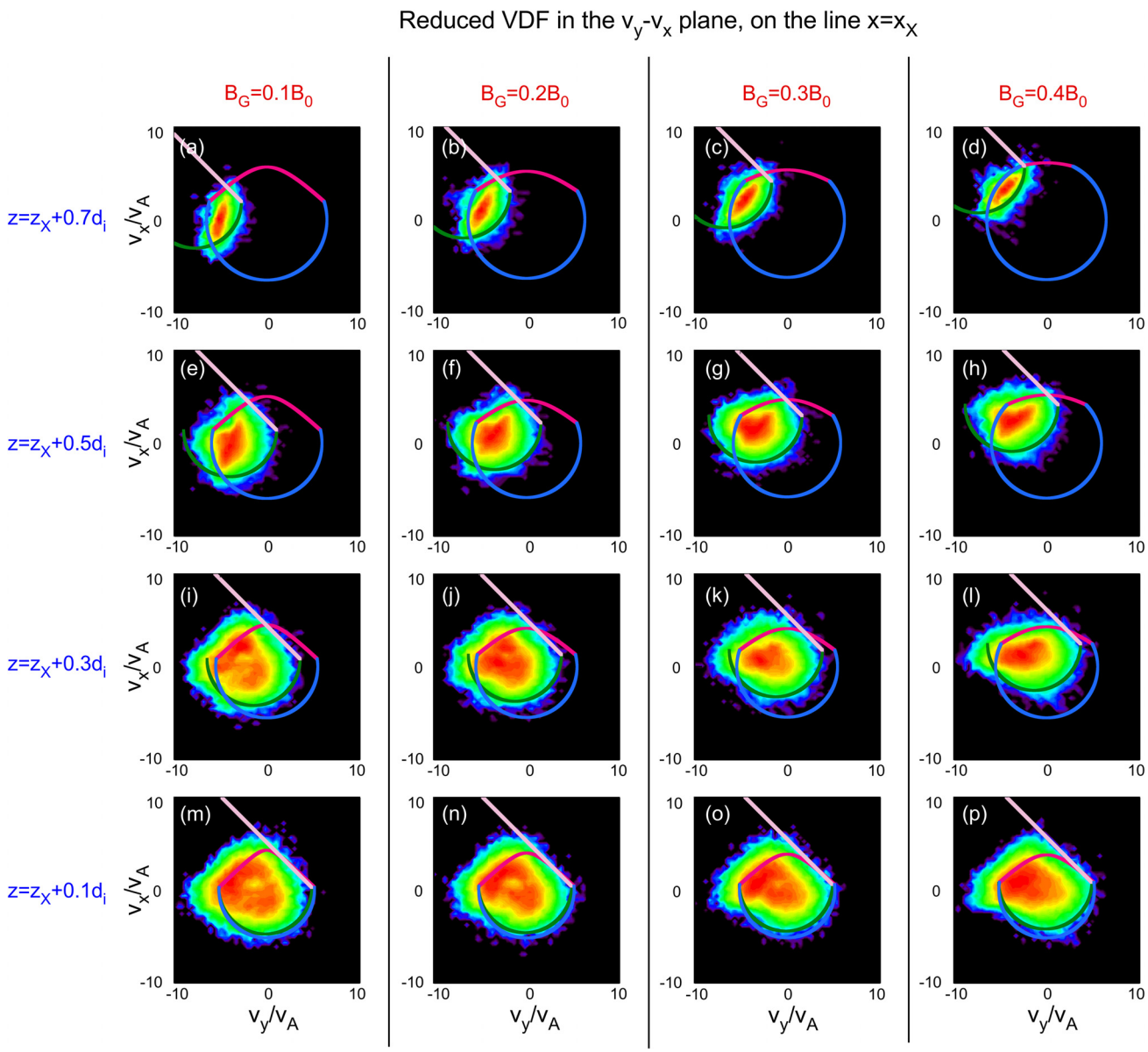

FIG. 10. Dependence of reduced VDFs in the v_y-v_x plane on z positions and various guide field strength ($0.1B_0$ to $0.4B_0$). Four theoretical curves (magenta, pink, blue, and green) are Eqs. (25)–(28), respectively. Translational mapping can explain each shape of the reduced VDF.

IV. THEORY OF ELECTRON VDFS IN GENERAL x-z POSITIONS

A. Reduced VDF in the velocity plane perpendicular to the magnetic field

We have discussed so far the boundaries of crescent VDFs along $x=0$, where the normal magnetic field, B_z, is zero. The theory in Sec. III is based on a 1-D model with $B_z=0$, and this approximation is valid around $x=0$. However, in a general x-z position in the EDR at a nonzero x position, the crescent structure in the v_y-v_z plane is slightly deformed (data not shown) from the one expressed in Eq. (17) as we move away from the $x=0$ line, because of the normal magnetic field B_z, which is an increasing function of x. In other words, the gyration around B_z and the parallel motion along B_z will modify the shape of a VDF in the v_y-v_z plane.

If $|B_z|$ in the EDR is much smaller than $|B_x|$, the effects of the gyration and the parallel motion due to B_z are considered secondary effects, and we expect that the same crescent structure perpendicular to the magnetic field holds in a general x position in the EDR. In this section, we will derive a theory to describe a VDF in a general x-z

Published under license by AIP Publishing

position under such a case. We will use the velocity plane perpendicular to the magnetic field, denoted by the $v_{\perp 1}$-$v_{\perp 2}$ plane, the same field-aligned coordinates used in space observations, such as Refs. 9, 10, 13, and 14. We define vectors $\boldsymbol{v}_{\perp 1}$ and $\boldsymbol{v}_{\perp 2}$ as $\boldsymbol{v}_{\perp 1} = \boldsymbol{b} \times (\boldsymbol{V}_e \times \boldsymbol{b})$ and $\boldsymbol{v}_{\perp 2} = -\boldsymbol{V}_e \times \boldsymbol{b}$, respectively, with $\boldsymbol{b}$ the unit vector parallel to the magnetic field, and the electron fluid velocity $\boldsymbol{V}_e$. The velocity components $v_{\perp 1}$ and $v_{\perp 2}$ for a particle are obtained as $v_{\perp 1} = \boldsymbol{v_p} \cdot \boldsymbol{v}_{\perp 1}/|\boldsymbol{v}_{\perp 1}|$ and $v_{\perp 2} = \boldsymbol{v}_p \cdot \boldsymbol{v}_{\perp 2}/|\boldsymbol{v}_{\perp 2}|$, respectively, where $\boldsymbol{v}_p$ is particle's velocity.

Before discussing VDFs in general positions, let us derive the form of the VDFs at $x = 0$ in the $v_{\perp 1}$-$v_{\perp 2}$ plane. We rotate a coordinate system v_x-v_y into v_{xr}-v_{yr} around the v_z axis, where the subscript r represents the rotated system. Since the region we discuss is near the electron stagnation point, the fluid velocity V_{ez} is negligibly small compared with other components. Neglecting V_{ez}, we rotate the coordinates v_x-v_y around the v_z axis, so that v_{xr} becomes $v_\parallel$, the velocity parallel to the magnetic field, which results in v_{yr} and v_{zr} being $-v_{\perp 1}$ and $-v_{\perp 2}$, respectively. Note that $v_{zr} = v_z$, and see Fig. 11(a) for this rotation. The relationship between the original v_x-v_y coordinates and the v_{xr}-v_{yr} coordinates is

$$v_{xr} = v_x \cos\theta + v_y \sin\theta, \tag{29}$$

$$v_{yr} = -v_x \sin\theta + v_y \cos\theta, \tag{30}$$

where θ is the angle between the v_x axis and the magnetic field $\boldsymbol{B}$, i.e., $\cos\theta = B_x/B$ and $\sin\theta = B_g/B$, where $B = (B_x^2 + B_g^2)^{1/2}$. Note that B_z is zero at $x = 0$. Using the above rotation, let us obtain the shape of a reduced VDF at $x = 0$, the same reduced VDF as discussed in Eq. (17), in the $v_{\perp 1}$-$v_{\perp 2}$ plane. The velocity v_x is obtained from Eq. (5), changing the inequality to the equality, and v_y satisfies Eq. (17). Using the expression of v_y in Eq. (17) as a function of v_z, we can express v_x obtained from Eq. (5) as a function of v_z. We substitute these v_x and v_y, expressed as functions of v_z, to Eq. (30) to obtain the relationship between v_{yr} and v_{zr}, considering the relationship $v_z = v_{zr}$. Since $v_{yr} = -v_{\perp 1}$ and $v_{zr} = -v_{\perp 2}$, we obtain the relationship between $v_{\perp 1}$ and $v_{\perp 2}$ as follows:

$$v_{\perp 1} = \frac{bz_{sp}}{2B_g}\left(v_y - \frac{m}{eb} z_{sp}^{-2} v_{\perp 2}^2 + \frac{1}{4}\frac{eb}{m} z_{sp}^2 + \frac{k}{b} - 2\frac{k}{b}\frac{z_c}{z_{sp}} + \frac{eB_g}{m}\frac{B_g}{b}\right)\sin\theta - v_y \cos\theta, \tag{31}$$

where v_y is given as Eq. (17), replacing v_z with $-v_{\perp 2}$. Note that we can obtain the same $v_{\perp 1}$-$v_{\perp 2}$ relationship in a different way, similar to the derivation of Eq. (17), by converting v_x and v_y in Eqs. (5) and (11) into v_{xr} and v_{yr} using Eqs. (29) and (30), and then eliminating v_{xr} $(=v_\parallel)$ in the system of equations to obtain the v_{yr}-v_{zr} relation, equivalently the $v_{\perp 1}$-$v_{\perp 2}$ relation, which is expressed as a more complex equation than Eq. (31), as seen in Appendix B, Eq. (B3). We numerically confirmed that Eqs. (31) and (B3) represent exactly the same curve.

Figure 11(g) shows an example of a VDF in the $v_{\perp 1}$-$v_{\perp 2}$ plane at $z = z_X + 0.45d_i$ and $x = x_X$, corresponding to $x = 0$ in the theory. We converted the velocity plane from the v_x-v_y-v_z coordinates to the $v_\parallel$-$v_{\perp 1}$-$v_{\perp 2}$ coordinates; therefore, the crescent appears in the right side of the $v_{\perp 1}$-$v_{\perp 2}$ plane. The theoretical curve of Eq. (31) is drawn as the magenta curve, and the theory and simulation are in good agreement.

Now, let us discuss crescent electrons at a finite x position. First, we consider a mapping of a reduced VDF in the $v_{\perp 1}$-$v_{\perp 2}$ at $x = 0$ to a position $x = x_r > 0$, right side of the X-line. To reach the region $x > 0$, particles at $x = 0$ need to have a positive v_x. As seen in the derivation of Eq. (17), the crescent boundary at $x = 0$ is determined by particles with $v_{x0} > 0$, i.e., $v_x > (eB_g/m)z_{sp}$, which is derived from Eq. (1). As long as the position $z = z_{sp}$ is positive in the magnetospheric side, the particles that determine the crescent boundary moves in the region $x > 0$. Therefore, this boundary Eq. (17) at $x = 0$ due to particles with $v_x > 0$ can be mapped into the reduced VDF at $x = x_r > 0$. If there is no B_z in the $x > 0$ region, we expect that there is an identity mapping of the VDF from $x = 0$ to a position $x = x_r > 0$. If there is a small B_z, which is a linear function of x, electrons gyrate around B_z; however, we expect that meandering motion is almost the same as the zero B_z case, but the plane of the meandering is perpendicular to the local magnetic field, which is the $v_{\perp 1}$-$v_{\perp 2}$ plane. The simulations show that $|B_z|$ in $|x - x_X| < 1.0d_i$ in the EDR is about an order of magnitude smaller than B_x at the z-directional edge $(z > z_X)$ of the EDR; therefore, we can treat the meandering motion almost the same as the zero B_z case, and only rotate the meandering into the $v_{\perp 1}$-$v_{\perp 2}$ plane. In other words, we assume that there is, approximately, an identity mapping of the VDF in the $v_{\perp 1}$-$v_{\perp 2}$ plane from $x = 0$ to $x = x_r$. Under this assumption, Eq. (31) represents the crescent boundary of the reduced VDF in the $v_{\perp 1}$-$v_{\perp 2}$ plane in a general x-z position, but $x > 0$, of the EDR.

In the above discussion, we consider a mapping from the VDF at $x = 0$ to $x = x_r$ using only particles with $v_x > 0$. In reality, the VDF at $x = x_r$ is composed of particles not only with $v_x > 0$, which come from $x = 0$ and also $0 < x < x_r$, but also particles with $v_x < 0$, which come from the region $x > x_r$. We will see later in the simulation result that the effect of the particles from $x > x_r$ with $v_x < 0$ on the crescent boundary of the VDF at $x = x_r$ is negligibly small, and using only $v_x > 0$ particles as in the above-mentioned mapping is sufficient to explain the crescent at $x = x_r$.

Next, we will discuss a reduced VDF in the $v_{\perp 1}$-$v_{\perp 2}$ plane at a position $x = x_l < 0$, left side of the X-line. If we consider a mapping from $x = 0$ to $x = x_l (< 0)$, only particles with negative v_x at $x = 0$ can reach the region $x < 0$. Since the boundary determined by Eq. (17) is due to particles with positive v_x, in order to discuss the boundary of a VDF at $x = x_l < 0$, we need to replace Eq. (17) with a different boundary curve determined by particles with $v_x < 0$, which will be substituted into Eq. (30).

The new crescent boundary due to particles with $v_x < 0$ is obtained by applying a similar way to derive Eq. (17). The reason why the crescent boundary by Eq. (17), for a reduced VDF of particles with $v_x > 0$, is different from the parabola represented by Eq. (5), for a v_x-cut of a VDF, is because the radius of the cross section circle, Eq. (7), decreases as v_x increases, while the parabola Eq. (5) is shifted rightward, as seen in Figs. 7(e) and 7(f). For negative v_x particles, as $|v_x|$ increases (v_x decreases), the radius of the cross section circle also decreases, as seen in Figs. 11(b) and 11(c), but the parabola Eq. (5) is shifted leftward, as seen in Fig. 11(d). Therefore, the crescent boundary in the v_y-v_z plane is determined by the rightmost boundary curve of Eq. (5), which corresponds to the curve of Eq. (5) with $v_x = 0$.

To see this, and to understand how the VDF boundary is determined by particles with $v_x < 0$, let us discuss more details based on Figs. 11(b)–11(d). Figure 11(b) shows the X-line VDF at $z = 0$ in the v_{y0}-v_{x0}, where three dashed lines are three cuts of the VDF at constant $v_{x0} (< 0)$. Each cut has a circular cross section. The top dashed line is at $v_{x0} = -1.75v_A$, which maps to $v_x = 0$ at $z = z_{sp} = 0.4d_i$, and

Published under license by AIP Publishing

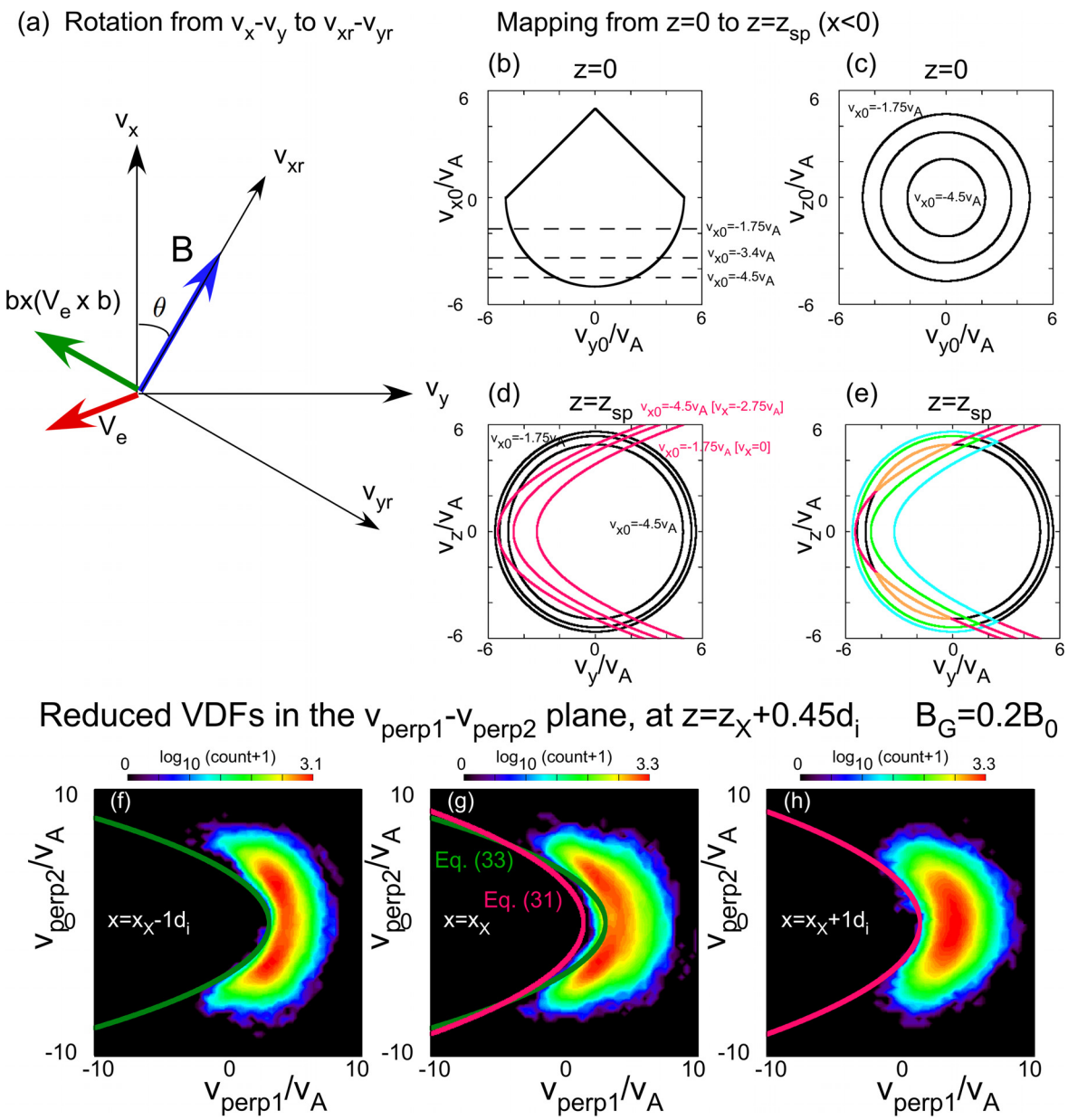

FIG. 11. (a) Rotation from v_x-v_y to v_{xr}-v_{yr}. The angle θ is between the v_x axis and the magnetic field $\boldsymbol{B}$. The v_{xr} axis is parallel to the magnetic field, and the v_{yr} axis is parallel to $-\boldsymbol{b} \times (\boldsymbol{V}_e \times \boldsymbol{b})$. (b)–(e) Mapping from $z = 0$ to $z = z_{sp}$ for particles in $x < 0$. (b) and (c) X-line VDF. Three dashed lines in (b) are cuts in various v_{x0} planes. Cross sections in those cuts are shown in (c). (d) and (e) Mapped cross sections at $z = z_{sp}$. Three circles correspond to the original circles at $z = 0$. Three magenta parabolas are Eq. (5) based on corresponding v_x. Panel (e) shows regions where electrons can exist. Since the light blue crescent includes the entire mapped crescents, the parabola boundary for $v_x = 0$ gives the boundary of the crescent electrons in $x < 0$. (f)–(h) Crescent VDFs in the velocity plane perpendicular to the magnetic field (in the $v_{\perp 1}$-$v_{\perp 2}$ plane) at $x = x_X - 1d_i$, $x = x_X$, and $x = x_X + 1d_i$, respectively, and $z = z_X + 0.45d_i$. Magenta curves are Eq. (31), while green curves are Eq. (33). There is asymmetry in the reduced VDF shape between the right side of the X-line (h) and the left side of the X-line (f).

the other two cuts, $v_{x0} = -3.4v_A$, and $-4.5v_A$, map to negative v_x-values, based on Eq. (1) using $z_{sp} = 0.4d_i$ and $B_g = 0.175B_0$ for run 2. Figure 11(c) shows the X-line VDF in the v_{y0}-v_{z0} plane, and the three circles correspond to the cross section at each v_{x0}-cut. In Fig. 11(d), the three circles are the mapped circles based on Eqs. (7) and (1), where $v_{r0}^2 + v_{x0}^2 = v_0^2$ with $v_0 = 5v_A$. The outermost circle is the one mapped from $v_{x0} = -1.75v_A$, and the innermost circle is the one mapped from $v_{x0} = -4.5v_A$. In addition to those circles, we plotted three parabolas, each of which corresponds to the parabola based on Eq. (5). The rightmost parabola is the one for $v_{x0} = -1.75v_A$,

Published under license by AIP Publishing

corresponding to $v_x = 0$, and the leftmost parabola is the one for $v_{x0} = -4.5v_A$. As $|v_{x0}|$ increases (v_{x0} decreases), the parabola is shifted leftward, and the radius of the mapped circle decreases. Electrons need to be within the region surrounded by the circle and the parabola in each v_x-cut plane, as seen in the light blue, light green, and orange curves in Fig. 11(e), and we see that the outermost region, surrounded by the light blue boundaries, determines the crescent of the reduced VDF. Therefore, the rightmost parabola, Eq. (5) by $v_x = 0$, corresponding to $v_{x0} = -1.75v_A$, represents the boundary of the VDF in the region $x < 0$.

Based on the above, to discuss a reduced VDF in the $v_{\perp 1}$-$v_{\perp 2}$ plane at $x = x_l < 0$, we will use Eq. (5) with $v_x = 0$, from which we obtain

$$v_y = \frac{m}{eb} z_{sp}^{-2} v_z^2 - \frac{1}{4}\frac{eb}{m} z^2 - \frac{k}{b} + 2\frac{k}{b}\frac{z_c}{z_{sp}} - \frac{eB_g}{m}\frac{B_g}{b}, \tag{32}$$

and we substitute this v_y and $v_x = 0$ into Eq. (30). As a result, after using $v_y = -v_{\perp 1}$ and $v_z = -v_{\perp 2}$, we obtain the crescent boundary in the $v_{\perp 1}$-$v_{\perp 2}$ plane at $x = x_l < 0$, due to particles with $v_x < 0$ as

$$v_{\perp 1} = -\left(\frac{m}{eb} z_{sp}^{-2} v_{\perp 2}^2 - \frac{1}{4}\frac{eb}{m} z_{sp}^2 - \frac{k}{b} + 2\frac{k}{b}\frac{z_c}{z_{sp}} - \frac{eB_g}{m}\frac{B_g}{b}\right)\cos\theta. \tag{33}$$

Again, we assume an identity mapping from $x = 0$ to $x = x_l < 0$, and we can use Eq. (33) to describe the crescent boundary of the reduced VDF in the $v_{\perp 1}$-$v_{\perp 2}$ plane in a general x-z position in $x < 0$.

In the above discussion for a VDF at $x = x_l < 0$, we consider a mapping from $x = 0$ to $x = x_l$, only using particles with $v_x < 0$. In reality, the VDF at $x = x_l < 0$ is composed of particles not only with $v_x < 0$, which come from $x = 0$ and also $x_l < x < 0$, but also particles with $v_x > 0$, which come from $x < x_l$. If the effect of particles with $v_x > 0$ coming from $x < x_l$ is significant, the boundary of the VDF at $x = x_l$ becomes different from Eq. (33). We will see later in simulation results that the effect of particles $v_x > 0$ on the boundary of the VDF at $x = x_l$ is minor, and the mapping by particles with $v_x < 0$ well explains the VDF at $x = x_l$.

Figures 11(f) and 11(h) show the reduced VDFs at $z = z_X + 0.45d_i$ and $x = x_X - 1.0d_i$, and $z = z_X + 0.45d_i$ and $x = x_X + 1.0d_i$, respectively. In the positive x side, Fig. 11(h), the boundary of the VDF is well explained by Eq. (31), drawn by the magenta curve. On the other hand, in the negative x side, Fig. 11(f), the boundary of the VDF matches Eq. (33), drawn by the green curve.

Figure 12 shows reduced VDFs in the $v_{\perp 1}$-$v_{\perp 2}$ plane in general x-z positions in the diffusion region for run 2 ($B_G = 0.2B_0$). The top panel shows the contour of E_z, and multiple red and pink boxes where VDFs are measured. The top right panel represents an example of a reduced VDF in the $v_{\perp 1}$-$v_{\perp 2}$ plane, where the magenta curve and the green curve represent the theoretical curves Eqs. (31) and (33), respectively, which are the mapping for the positive and the negative x regions, respectively. The multiple panels below the E_z panel show reduced VDFs in the $v_{\perp 1}$-$v_{\perp 2}$ plane, and each panel corresponds to the position of a red or a pink box in the top panel. The x positions are shown in the top of the multiple VDF panels, and the z positions are shown in the left panels. In each VDF, either the theoretical curve Eq. (31) or Eq. (33) is drawn, depending on whether the x position is in the positive side from the X-line, $x \geq x_X$, or the negative side, $x \leq x_X$. On the VDFs at $x = x_X$, both theoretical curves are drawn. To plot each VDF, we converted the coordinate system from v_x-v_y-v_z into $v_\parallel$-$v_{\perp 1}$-$v_{\perp 2}$, using local $\boldsymbol{V}_e$ and $\boldsymbol{b}$. There are matches between the theory and the boundaries of VDFs in red boxes, as seen in the top E_z plot, which reside outside the separatrices in the magnetospheric side of the EDR. The pink boxes are where the theory and the boundaries of VDFs show some disagreement, and those boxes are located, basically, on the separatrices in the magnetospheric side. In the VDF panels, the pink lines separate the group of VDFs in which the theory and the simulation have agreement (outside the separatrices) and the group in which the theory and the simulation have differences. The region of the red boxes, the outside of the separatrices, is where electrons are meandering; therefore, the theoretical curves and the VDFs show good agreement. In contrast, the region of pink boxes (inside those separatrices) is where outflows are generated, and reconnected field lines are convected from the X-line. In that region, we expect that there are many electrons that are not only meandering but also magnetized and moving along magnetic field lines. Since the theory assumes that all the electrons are unmagnetized in the EDR and they are meandering across the current sheet, the theory can be applied only to VDFs outside the separatrices, which is the region with red boxes.

Figure 13 shows reduced VDFs in the $v_{\perp 1}$-$v_{\perp 2}$ plane for run 4, which has a larger guide field $B_G = 0.4B_0$. There is agreement between the theory and simulation VDFs in the region outside the separatrices, corresponding to the red box region, while there are some discrepancies between them in the region near the separatrices, corresponding to the pink box region. However, compared with the case in Fig. 12 for $B_G = 0.2B_0$, there are a couple of different features. One is that the pink regions, where the theory does not match the boundaries of the VDFs, are not on the separatrices in the magnetospheric side of the EDR, but there are pink boxes slightly away from the separatrices, and the red region, where the theory matches the VDFs, becomes narrower in the x direction than that in a smaller guide field case, Fig. 12. Another difference between a case with a larger guide field $B_G = 0.4B_0$ and that with $B_G = 0.2B_0$ is that VDFs along $x = x_X - 0.5d_i$ do not match the theory of green curves, and there are many electrons inside the green crescent boundaries. Instead, one can say that they match the theory of magenta curves better, even though there are small gaps between the curves and the VDFs. The exact reason for these differences is still unknown; however, as we see in Subsection IV B and Fig. 16, the VDFs along $x = x_X - 0.5d_i$ contain small numbers of electrons with $v_x < 0$, and there are many $v_x > 0$ electrons, which were discussed when deriving the magenta theory curves. Therefore, the theory with $v_x > 0$, for magenta curves, works well in the region close to $x = x_X$ even slightly in the negative x side. The overall tendency that the theory agrees with simulation VDFs outside the separatrices holds in this large guide field case and in the small guide field case.

In both runs, Fig. 12 for run 2 ($B_G = 0.2B_0$) and Fig. 13 for run 4 ($B_G = 0.4B_0$), some VDFs show multiple components. For example, in Fig. 13 for run 4, double stripes along the crescent are seen in the VDFs at $(x,z) = (x_X + 0.5d_i, z_X + 0.25d_i)$, $(x_X + 1.0d_i, z_X + 0.25d_i)$, $(x_X + 0.5d_i, z_X + 0.35d_i)$, and $(x_X + 1.0d_i, z_X + 0.35d_i)$. Those multiple stripes may be due to acceleration by the reconnection electric field to the $v_{\perp 1}$-direction, perpendicular to the magnetic field, as discussed in Ref. 6. Also, three blobs are seen in the VDFs at $(x,z) = (x_X, z_X + 0.25d_i)$, $(x_X - 0.5d_i, z_X + 0.25d_i)$, and $(x_X - 1.0d_i, z_X + 0.25d_i)$, which may indicate that the acceleration history varies in each

Published under license by AIP Publishing

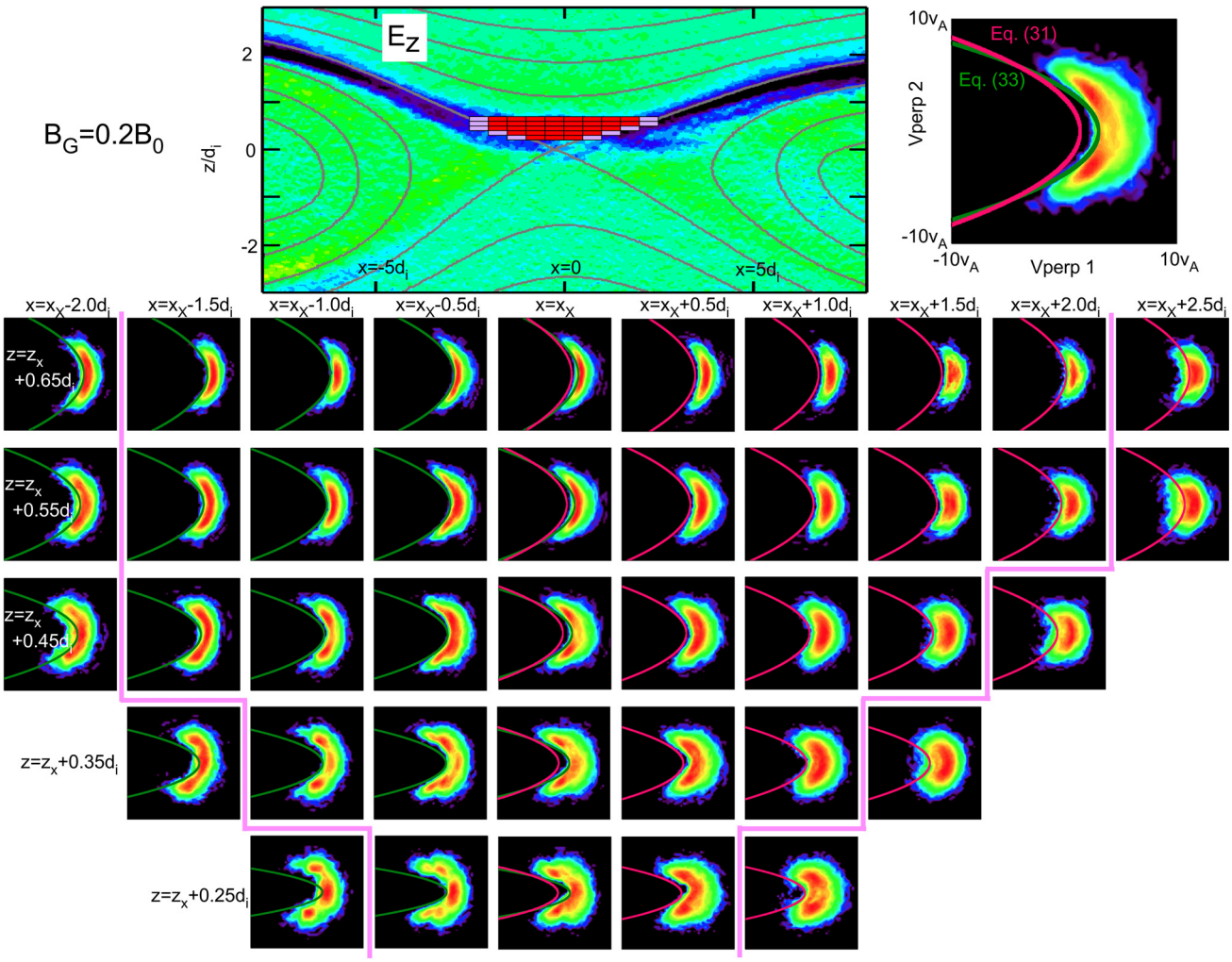

FIG. 12. Crescent boundaries in general *x*-*z* positions in run 2 ($B_G = 0.2B_0$). Top left: E_z contour and multiple regions where VDFs are measured (each box size is $0.5d_i$ in *x* and $0.1d_i$ in *z*). Red boxes are where theory and simulations are in good agreement, while pink boxes are where there are differences between theory and simulations. Top right: An example of a reduced VDF in the $v_{\perp 1}$-$v_{\perp 2}$ plane. The magenta curve is Eq. (31), and the green curve is Eq. (33). Lower multiple panels: Reduced VDFs in the $v_{\perp 1}$-$v_{\perp 2}$ plane. Pink lines between panels divide VDFs into the red box group and the pink box group. VDFs and theory are in good agreement (red box group) outside the magnetospheric separatrices.

component. Further studies by particle tracing in PIC simulations are necessary to understand these detailed structures in VDFs.

B. Cut of VDF in the $v_\perp$-$v_\parallel$ plane

Finally, let us focus on cuts of VDFs in the $v_{\perp 1}$-$v_\parallel$ plane, and discuss the guide field effect, the formation of a straight-line cut-off of a VDF nonparallel to the magnetic field. In Sec. III A, we showed that a cut of a VDF in the v_y-v_x plane has a straight-line cut-off, $v_y \sim (2B_g/B_x)v_x$, whose slope is twice larger than the slope determined by the direction parallel to the magnetic field B_g/B_x, and this is because electrons meander across the current sheet in a linearly increasing magnetic field $B_x = bz$. To derive that straight-line cut-off, Eq. (5) was applied only to VDFs on the line $x = 0$, but using the same concept, an identity mapping from $x = 0$ to a general x position, as in the previous Subsection IV A for reduced VDFs in the $v_{\perp 1}$-$v_{\perp 2}$ plane, let us discuss a cut of an VDF in the $v_{\perp 1}$-$v_\parallel$ plane in a general *x*-*z* position in the EDR.

We will convert the v_y-v_x coordinate into the $v_{\perp 1}$-$v_\parallel$ coordinate, based on Eqs. (29) and (30), using $v_{xr} = v_\parallel$, $v_{yr} = -v_{\perp 1}$, and $v_{zr} = -v_{\perp 2}$. From Eqs. (29) and (30), we obtain the reverse conversion relationship as

$$v_x = v_\parallel \cos\theta + v_{\perp 1} \sin\theta, \tag{34}$$

$$v_y = v_\parallel \sin\theta - v_{\perp 1} \cos\theta. \tag{35}$$

Substituting these Eqs. (34) and (35) into Eq. (5), we obtain the inequality for $v_{\perp 1}$ and $v_\parallel$ as

Published under license by AIP Publishing

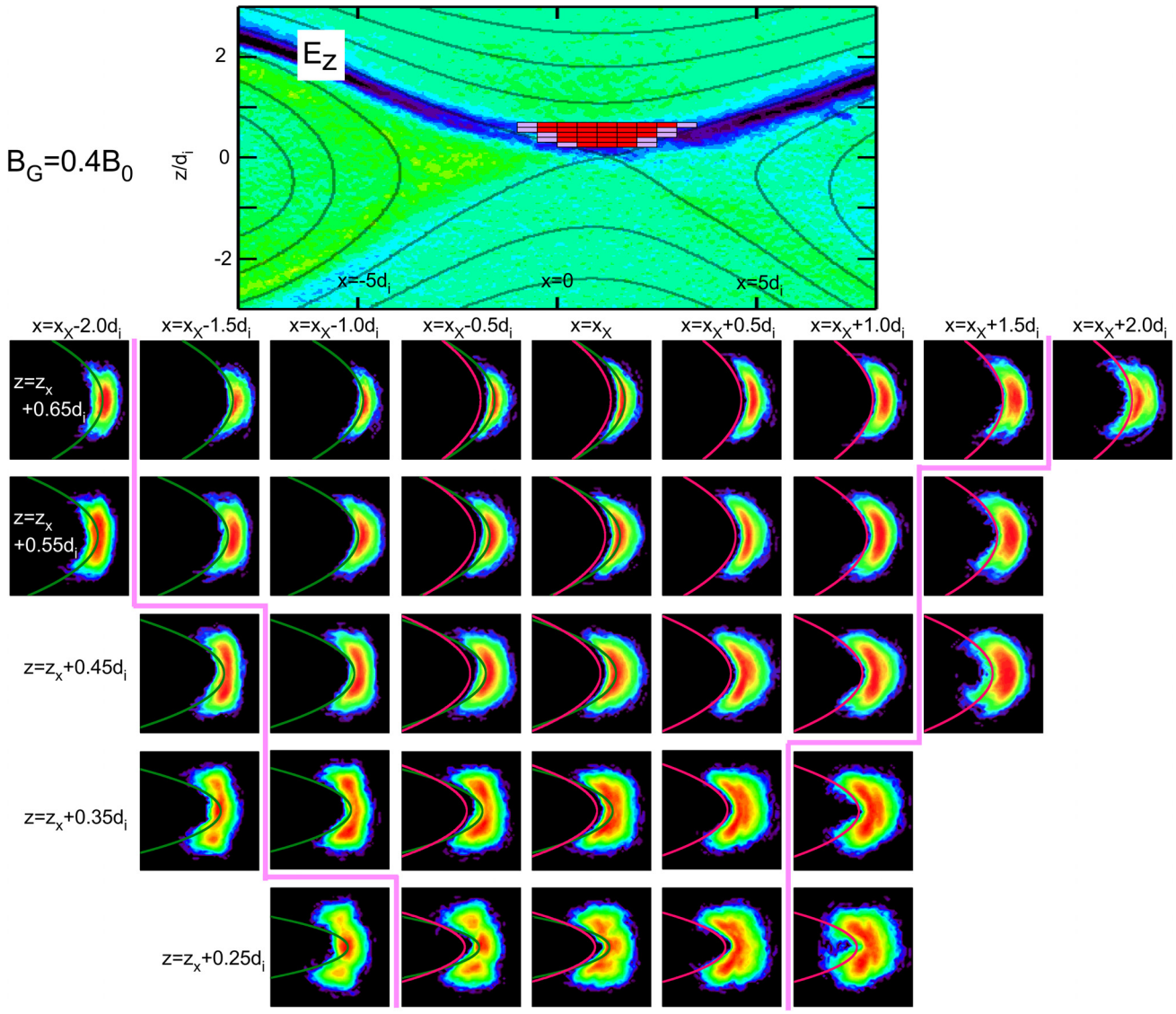

FIG. 13. Crescent boundaries in general *x*-*z* positions in run 4 ($B_G = 0.4B_0$). Same format as Fig. 12.

$$v_{\perp 1} \geq -\frac{2\frac{B_g}{bz_{sp}}\cos\theta - \sin\theta}{\cos\theta + 2\frac{B_g}{bz_{sp}}\sin\theta} v_{\parallel} - \frac{\frac{m}{eb}z_{sp}^{-2}v_{\perp 2}^2 - \frac{1}{4}\frac{eb}{m}z_{sp}^2 - \frac{k}{b} + 2\frac{k}{b}\frac{z_c}{z_{sp}} - \frac{eB_g}{m}\frac{B_g}{b}}{\cos\theta + 2\frac{B_g}{bz_{sp}}\sin\theta}, \tag{36}$$

where $\cos\theta$ and $\sin\theta$ are $\cos\theta = B_x/B$ and $\sin\theta = B_g/B$ with $B = (B_x^2 + B_g^2)^{1/2}$, respectively, and we replaced v_z with $-v_{\perp 2}$. Note that the denominator, $\cos\theta + 2(B_g/bz_{sp})\sin\theta$, is always positive if $z_{sp} > 0$. If we specify a $v_{\perp 2}$ value, Eq. (36) will give a straight-line cut-off of a VDF in the $v_{\perp 1}$-$v_{\parallel}$ plane. Equation (36) shows a straight line inclined from the $v_{\parallel}$ axis because electrons are meandering in a linearly increasing magnetic field $B_x = bz$, instead of gyrating around the magnetic field.

We here again assume an identity mapping from the cut of an VDF at $x = 0$ to a cut of an VDF with a finite x position. The mapping to the positive x region requires the condition that $v_x > 0$. From Eq. (34) and considering $v_x > 0$, we obtain the following condition for $v_{\parallel}$ and $v_{\perp 1}$ as

$$v_{\perp 1} > -v_{\parallel}\cot\theta. \tag{37}$$

Therefore, in the positive x region, both Eqs. (36) and (37) need to be satisfied. On the other hand, to discuss the negative x region, which requires $v_x < 0$, we obtain the condition from Eq. (34) as

Published under license by AIP Publishing

$$v_{\perp 1} < -v_{\parallel}\cot\theta. \tag{38}$$

In the negative x region, both Eqs. (36) and (38) need to be satisfied.

Figures 14(a)–14(c) compare the prediction by Eq. (36), drawn by the magenta lines, with simulation VDFs at $x = x_X - 1.0d_i$, $x = x_X$, and $x = x_X + 1.0d_i$, respectively, for $z = z_X + 0.45d_i$. They are the cuts of the same VDFs in Figs. 11(f)–11(h) at the $v_{\perp 2} = 0$ plane, using a particle velocity range $-0.5v_A \le v_{\perp 2} \le 0.5v_A$ to make these plots. In the panels (a) and (c), the lines for Eqs. (37) and (38) are plotted by the light blue lines. The theory Eq. (36) matches well the VDF at $x = x_X$ in panel (b). In panel (c) for the positive x side, the region determined by Eq. (37) is above the light blue line; therefore, meandering electrons should appear in the region above both the magenta line and the light blue line, which is the region with the solid light blue dot. The VDF at $x = x_X + 1.0d_i$ matches the theoretical prediction. Note that particles below the light blue line correspond to $v_x < 0$, which come from the region $x > x_X + 1.0d_i$, and their contribution to determine the crescent boundary, discussed in Subsection IV A, is minor, and negligible in this $v_{\perp 2} = 0$ case, and generally small in other $v_{\perp 2}$ planes as well as other x-z positions. In contrast, in panel (a) for the negative x side, the region determined by Eq. (38) is below the light blue line; therefore, meandering electrons should appear in the region above the magenta line, but below the light blue line, which is the region with the solid light blue dot in panel (a). In the region above the light blue line, which is the region excluded from Eq. (38), meandering electrons coming from $x > x_X - 1.0d_i$ should not appear. Therefore, we interpret that particles appearing above both the magenta curve and the light blue curve in panel (a) are either meandering particles from $x < x_X - 1.0d_i$ or magnetized electrons, which are gyrating along the magnetic field. Since the VDF in the velocity region above both the magenta line and the light blue line extends almost in the vertical direction, parallel to the magnetic field, these electrons may be magnetized to some degree and moving along the magnetic field. However, this component also has a positive constant $v_{\perp 1}$, and $v_{\perp 1}$ is much larger than the $E \times B$ drift speed, which is around $0.6v_A$ at this position. Therefore, they are not perfectly magnetized electrons. Overall, the three panels (a)–(c) indicate that the theoretical predictions by Eqs. (36)–(38) show agreement with VDFs in general positions of x.

Figures 15 and 16 show cuts of VDFs in the $v_{\perp 1}$-$v_{\parallel}$ plane in general x-z positions for run 2 ($B_G = 0.2B_0$) and run 4 ($B_G = 0.4B_0$), respectively, for the z positions $z = 0.35d_i$ and $z = 0.65d_i$. The $v_{\perp 2}$ value is shown in each panel, and the range of $v_{\perp 2}$ is $\pm 0.5v_A$ around the specified $v_{\perp 2}$. The magenta lines represent Eq. (36), and the light blue lines represent Eqs. (37) or (38). In the positive and the negative x regions, the velocity domain indicated by a light blue dot is where the theory predicts that meandering particles exist. In Fig. 15, most particles in the velocity domain indicated by a light blue dot in each panel are bounded by the theoretical lines. However, a large number of particles appear outside the predicted boundaries on the negative side of the X-line, $x < x_X$, for a higher $B_g = 0.4B_0$ (run 4) as shown in Fig. 16. In this negative domain, there are electrons along the vertical direction with a constant positive $v_{\perp 1}$, suggesting partially magnetized electrons, mainly above the light-blue-dot region. This tendency is conspicuous at $x = x_X - 1.0d_i$, and the parallel extending component appears even in the light-blue-dot region in some panels. In run 4 ($B_G = 0.4B_0$, Fig. 16), the negative x region shows small numbers of electrons in the light-blue-dot regions, corresponding to $v_x < 0$. At $x = x_X - 1.0d_i$, most of the electrons appear as the parallel extending component, with a constant $v_{\perp 1}$, above the light-blue-dot regions. This suggests that in a larger guide field run (run 4), many electrons in the negative x region are coming from the left to each VDF measurement point, with $v_x > 0$, not from the right side including the X-line, with $v_x < 0$. At $x = x_X - 0.5d_i$, in the region above the light blue dot, electrons are not aligned parallel to the magnetic field, but they extend along the magenta theoretical curve, suggesting that they are unmagnetized and meandering across the current sheet. Since they appear above the light-blue-dot regions, they are not from the X-line, with $v_x < 0$, but from the left to each VDF measurement point with $v_x > 0$. Therefore, if we look into the VDF in the $v_{\perp 1}$-$v_{\perp 2}$ in Fig. 13, the crescent boundary in each panel at $x = x_X - 0.5d_i$ does not match the green theoretical curve, Eq. (33), which assumes electrons with $v_x < 0$, but match the magenta theoretical curve, Eq. (31), which assumes electrons with $v_x > 0$.

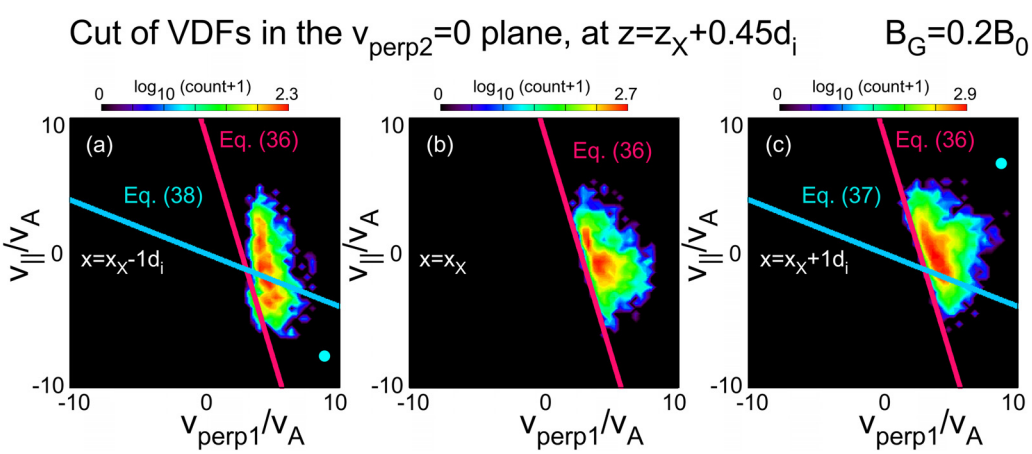

FIG. 14. (a)-(c) Cuts of VDFs in the velocity plane coplanar with the magnetic field (in the $v_{\perp 1}$-$v_{\parallel}$ plane) at $x = x_X - 1d_i$, $x = x_X$, and $x = x_X + 1d_i$, respectively, and $z = z_X + 0.45d_i$. Magenta lines are Eq. (36), and light blue lines are Eqs. (37) and (38). The closed light blue dot indicates the region where electrons from $x = 0$ can reach. Panels (b) and (c) show agreement between the theory and the VDFs. Panel (a) shows a vertical (parallel) component above the light blue line.

Published under license by AIP Publishing

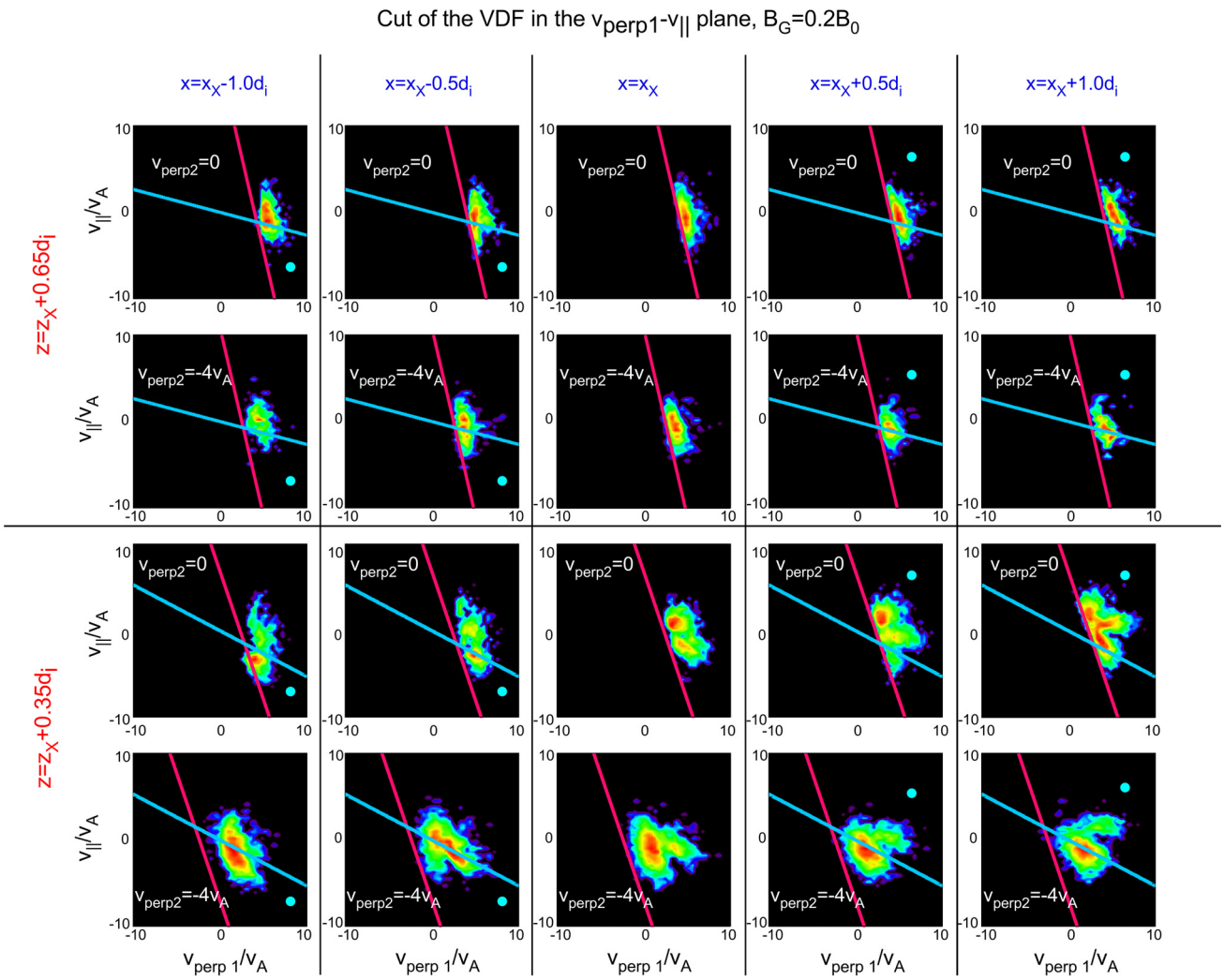

FIG. 15. Cuts of VDFs in the $v_{\perp 1}$-$v_{\parallel}$ plane in general *x*-*z* positions for run 2 ($B_G = 0.2B_0$). Top two rows: cuts of VDFs at $z = z_X + 0.65d_i$, for $v_{\perp 2} = 0$ and $-4v_A$. The bin size to measure VDFs is $0.5d_i$ in *x* and $0.1d_i$ in *z*. Bottom two rows: Cuts of VDFs at $z = z_X + 0.35d_i$, for $v_{\perp 2} = 0$ and $-4v_A$. Magenta lines are Eq. (36), while light blue lines are Eqs. (37) and (38). The light blue dot represents the region where electrons from $x = 0$ can reach. In the positive *x* region, theory and simulations agree well. In the negative *x* region, there are vertical (parallel) components in the velocity region above the region with the light blue dot.

In Table II, to facilitate comparisons of our theoretical and simulation results with space observations of electron distribution functions from magnetopause diffusion regions, we summarize all the obtained theoretical VDF boundaries for meandering electrons in this study, using *L*-*M*-*N* coordinates by minimum variance analysis,[23] where *L* is the outflow direction, *M* is the out-of-plane direction, and *N* is the direction normal to the current sheet. The coordinates *L*, *M*, and *N* correspond to *x*, *y*, and *z*, respectively, and $B_L > 0$ in $N > 0$.

In the theory, we assume that the guide field strength is not too large, in the range $0.5B_0 > B_g$. If the guide field strength is much larger than $0.5B_0$, we expect that electrons become more magnetized than those in this study, and the theory obtained in this paper may need modification. Roughly speaking, the threshold of the guide field can be estimated as follows. When electron meandering motion is dominant compared with the gyromotion in the guide field, an inequality $(ebv_0/m)^{1/2} > eB_g/m$ is expected to be satisfied, where the left-hand side is the characteristic frequency of the meandering motion (see Eq. (17) in Ref. 6), and the right-hand side is the gyro frequency in the guide field. The velocity v_0 is a typical meandering speed at $z = 0$. Substituting simulation values of $b \sim 1B_0/d_i$ based on Table I, $v_0 \sim 5v_A$ based on the X-line distribution in Fig. 2, and $m_i/m_e = 25$ used in this study, we obtain that $0.45B_0 > B_g$. We expect that if B_g is much greater than 50% of the reconnecting field, the gyration effect due to B_g dominates over the meandering motion in B_x, and the theory may need modification. Note that in the above estimate, fixed values of b and v_0 are used under a fixed mass ratio. Further studies are needed to obtain a precise guide field threshold.

Published under license by AIP Publishing

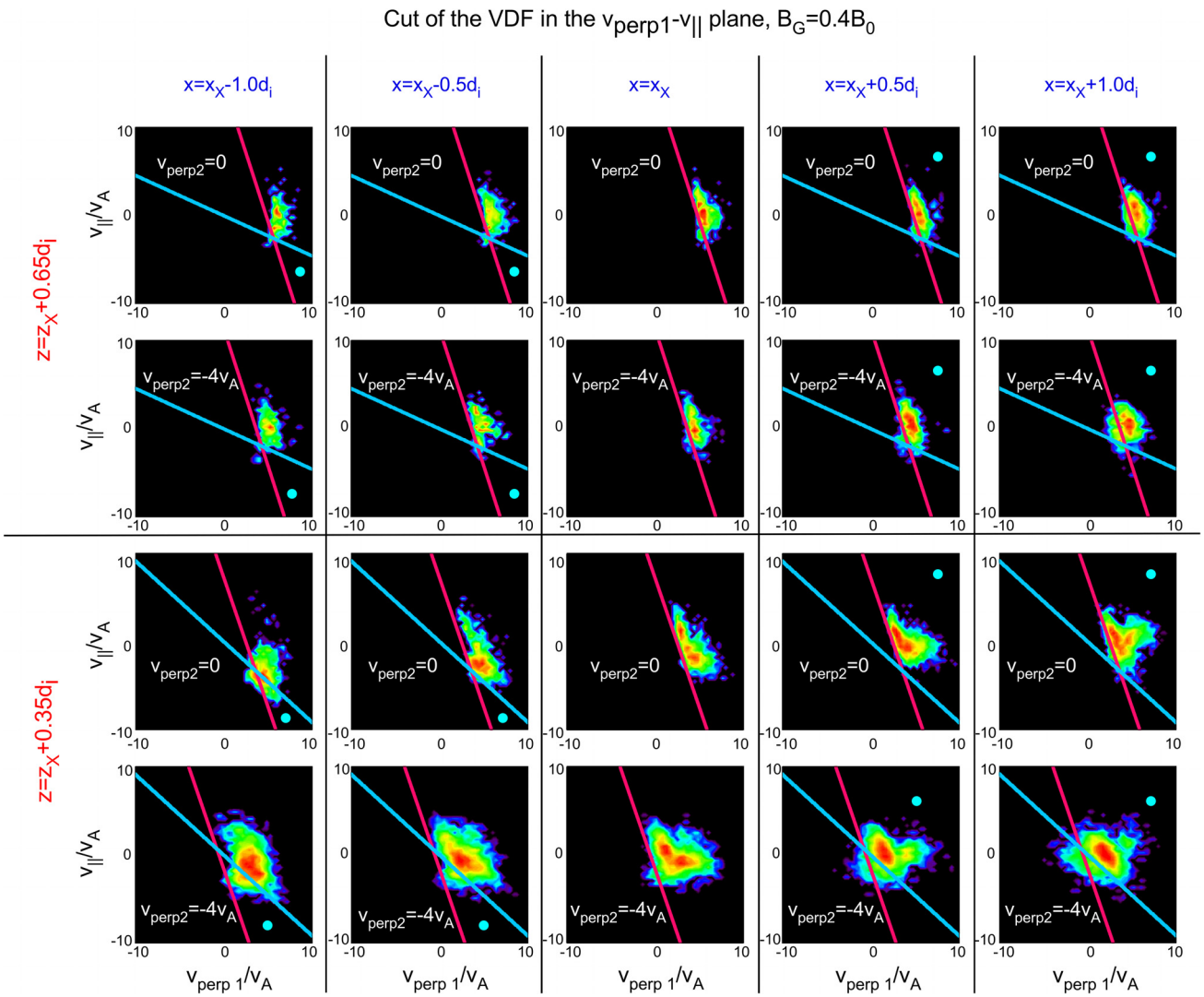

FIG. 16. Cuts of VDFs in the $v_{\perp 1}$-$v_{\parallel}$ plane in general *x*-*z* positions for run 4 ($B_G = 0.4B_0$). Same format as Fig. 15.

TABLE II. Summary of the theory to compare with the space observation data.

Distribution cuts, along the $L = 0$ line	
Cut of VDF in the v_M-v_N plane at $v_L = v_{La}$	$v_M \leq \frac{m}{eb} N^{-2} v_N^2 - \frac{1}{4}\frac{eb}{m} N^2 - \frac{k}{b} + 2\frac{B_g}{bN}\left(v_{La} + \frac{kN_c}{B_g}\right) - \frac{eB_g}{m}\frac{B_g}{b}$ See Eq. (5) and Fig. 4
Cut of VDF in the v_M-v_L plane at $v_N = v_{Na}$	$v_M \leq 2\frac{B_g}{bN} v_L + \frac{m}{eb} N^{-2} v_{Na}^2 - \frac{1}{4}\frac{eb}{m} N^2 - \frac{k}{b} + 2\frac{k}{b}\frac{N_c}{N} - \frac{eB_g}{m}\frac{B_g}{b}$ See Eq. (5) and Fig. 5

Published under license by AIP Publishing

TABLE II. (*Continued.*)

Reduced distributions, along the $L = 0$ line	
Reduced VDF in the v_M-v_N plane	$v_M \le -\frac{A_1}{A_0} - \frac{\left[A_1^2 - A_0\left(A_1^2 - A_2\right)\right]^{1/2}}{A_0}$ where $A_0 = \left[1 - 4s^2\left(\frac{B_g}{bN}\right)^2\right]$ $A_1 = -\frac{m}{eb}N^{-2}v_N^2 + \frac{1}{4}\frac{eb}{m}N^2 - 2s\frac{B_g}{bN}v_0 - (2s^2+1)\frac{eB_g}{m}\frac{B_g}{b} - 2\frac{k}{b}\frac{N_c}{N} + \frac{k}{b}$ $A_2 = 4s^2\left(\frac{B_g}{bN}\right)^2\left[2s\frac{eB_g}{m}Nv_0 + (s^2+1)\left(\frac{eB_g}{m}\right)^2N^2 - \frac{ek}{m}\left(N^2 - 2N_cN\right) + v_N^2\right]$ See Eq. (17) and Fig. 8
Reduced VDF in the v_M-v_L plane	For the region $v_L \ge (eB_g/m)N$: $\left[s^{-1}v_L - v_0 - s^{-1}(s^2+1)\frac{eB_g}{m}N\right]^2 - v_M^2 \ge 2sv_0\frac{eB_g}{m}N + (s^2+1)\left(\frac{eB_g}{m}\right)^2N^2 - \frac{ek}{m}\left(N^2 - 2N_cN\right)$ $v_L - sv_0 - \frac{eB_g}{m}N - s\frac{eb}{2m}N^2 \le sv_M \le -v_L + sv_0 + \frac{eB_g}{m}N - s\frac{eb}{2m}N^2$ For the region $v_L < (eB_g/m)N$: $v_L^2 + v_M^2 \le v_0^2 + \frac{ek}{m}\left(N^2 - 2N_cN\right)$ $v_L \ge -\left[v_0^2 - \left(v_M + \frac{eb}{2m}N^2\right)^2\right]^{1/2} + \frac{eB_g}{m}N$ See Eqs. (25), (26), (27) and (28) and Fig. 10
Distributions in a general L position	
Reduced VDF in the $v_{\perp 1}$-$v_{\perp 2}$ plane	For $L > 0$: $v_{\perp 1} \ge \frac{bN}{2B_g}\left(v_M - \frac{m}{eb}N^{-2}v_{\perp 2}^2 + \frac{1}{4}\frac{eb}{m}N^2 + \frac{k}{b} - 2\frac{k}{b}\frac{N_c}{N} + \frac{eB_g}{m}\frac{B_g}{b}\right)\sin\theta - v_M\cos\theta$ where v_M is given in the row "Reduced VDF in the v_M-v_N plane" (with the equal sign). See Eq. (31) and Fig. 11(h). For $L < 0$: $v_{\perp 1} \ge -\left(\frac{m}{eb}N^{-2}v_{\perp 2}^2 - \frac{1}{4}\frac{eb}{m}N^2 - \frac{k}{b} + 2\frac{k}{b}\frac{N_c}{N} - \frac{eB_g}{m}\frac{B_g}{b}\right)\cos\theta$ See Eq. (33) and Fig. 11(f).
Cut of VDF in the $v_{\perp 1}$-$v_{\parallel}$ plane at $v_{\perp 2} = v_{\perp 2a}$	$v_{\perp 1} \ge -\frac{2\frac{B_g}{bN}\cos\theta - \sin\theta}{\cos\theta + 2\frac{B_g}{bN}\sin\theta}v_{\parallel} - \frac{\frac{m}{eb}N^{-2}v_{\perp 2a}^2 - \frac{1}{4}\frac{eb}{m}N^2 - \frac{k}{b} + 2\frac{k}{b}\frac{N_c}{N} - \frac{eB_g}{m}\frac{B_g}{b}}{\cos\theta + 2\frac{B_g}{bN}\sin\theta}$ and $v_{\perp 1} > -v_{\parallel}\cot\theta$ in $L > 0$, or $v_{\perp 1} < -v_{\parallel}\cot\theta$ in $L < 0$ See Eqs. (36), (37) and (38) and Fig. 14

V. CONCLUSION

We have studied electron VDFs, focusing on meandering electrons from the magnetosheath, in the EDR of asymmetric reconnection with guide fields. The effects of a guide field on crescent electron VDFs due to meandering electrons are summarized as follows: (1) A guide field changes the v_y-intercept of the crescent-shaped boundary in a v_x-cut of a VDF. (2) Because of a guide field and meandering motion, a v_z-cut of an VDF has a linear line cut-off whose slope is nonparallel to the local magnetic field. (3) A reduced VDF integrated

Published under license by AIP Publishing

along v_x shows a larger opening angle of the crescent under a guide field, compared with a zero-guide field case. The dependence of the crescent opening angle in a reduced VDF on a guide field is more noticeable than the dependence of the v_y-intercept in a cut of a VDF. (4) A reduced VDF integrated along v_z shows a translational mapping from the VDF at the X-line, in which the translational direction is perpendicular to the cut-off line of a v_z-cut of a VDF. (5) In general positions of x-z, crescent electron VDFs perpendicular to the magnetic field show an identity mapping from VDFs at $x = 0$, as long as the position is outside the magnetospheric separatrices. (6) In general positions of x-z, the cut of an VDF with a constant perpendicular velocity (a constant $v_{\perp 2}$) shows a linear cut-off that is not parallel to the magnetic field, and an identity mapping is seen.

The above results are useful for space measurements of EDRs of reconnection by spacecraft in Earth's magnetosphere, such as NASA's MMS mission. There are a number of EDR events observed by MMS, with various strengths of guide fields, and we expect that our theoretical predictions of the boundary shapes of crescent electron VDFs can be applied to those events. In this study, we have derived theoretical prediction curves for general positions in the x-z plane, which is one of the major advancements over our previous studies focusing on the $x = 0$ line. In this study, we have investigated up to the strength of a guide field 40% of the asymptotic magnetic field, and we have confirmed that within this range of the guide field, our theory is valid if reconnection is laminar.

Furthermore, we have newly shown that meandering electrons exhibit a VDF cut-off nonparallel to the magnetic field, as explained in the above summaries (2) and (6), about the cut of an VDF in the v_y-v_x plane with a constant v_z or the $v_\parallel$-$v_{\perp 1}$ plane with a constant $v_{\perp 2}$. This feature will be useful to identify meandering and unmagnetized electrons in an EDR to distinguish a crescent VDF structure due to meandering from the ones due to magnetized electrons.[22] If we observe a crescent electron VDF with a slope, in the velocity plane coplanar with a magnetic field, different from the magnetic field direction, they can be unmagnetized meandering electrons.

ACKNOWLEDGMENTS

This work was supported by DOE Grant No. DESC0016278, NSF Grant Nos. AGS-1619584 and AGS-1552142, NASA Grant No. 80NSSC18K1369, and the NASA MMS project. The work at the University of Bergen was supported by the Research Council of Norway/CoE under Contract No. 223252/F50. The simulation data are available upon request from the authors.

APPENDIX A: THE CONDITION FOR v_{zd0} TO DERIVE EQ. (5)

To derive Eq. (5), we applied the condition $v_{zd0}^2 \geq 0$ to Eq. (4). The crescent boundary of a VDF, which is a parabola represented by Eq. (5), is determined by the particles with $v_{zd0} = 0$. However, this condition is valid only for $v_{xd0} < 0$, which is seen in the discussion below, and we need to use a different condition $v_{zd0}^2 \geq c_z$ when $v_{xd0} \geq 0$, where c_z is a positive function of v_{xd0} and v_{yd0}. In this section, we will derive this c_z, and show that the correction to the curve Eq. (5) due to c_z is minor and can be neglected.

Since there is a guide field $B_y = B_g$, the magnetic force in the z direction for an electron at $z = 0$ is $-ev_{xd0}B_g$ in the drifting frame, where E_z disappears. When $v_{xd0} < 0$, this force is positive; therefore, particles $v_{zd0} = 0$ can move into the region $z > 0$. However, if $v_{xd0} \geq 0$, the force $-ev_{xd0}B_g \leq 0$, and the particles with $v_{zd0} = 0$ cannot enter the region $z > 0$. Therefore, when $v_{xd0} \geq 0$, the particles with $v_{zd0} = 0$ cannot determine the parabolic boundary Eq. (5), but there should be a lower limit of $v_{zd0}(> 0)$ that constitutes the crescent boundary of a VDF.

Let us obtain c_z, which is the lower bound of v_{zd0}^2 for the crescent boundary, from the z motion of particles. From Eq. (4), using Eqs. (1) and (2), we obtain the following:

$$v_{zd}^2 + U(z) = 0, \tag{A1}$$

where $U(z)$ represents a quartic potential for z, defined as

$$U(z) = \frac{1}{4}\left(\frac{eb}{m}\right)^2 z^4 - \left(\frac{eb}{m}\right)\left(v_{yd0} - \frac{eB_g}{m}\frac{B_g}{b}\right)z^2 + 2\frac{eB_g}{m}v_{xd0}z - v_{zd0}^2, \tag{A2}$$

and we omitted the subscript d for position z. For particles to enter $z > 0$ and reach $z = z_{sp}$, $v_{zd}^2 \geq 0$ needs to be satisfied in the range $0 \leq z \leq z_{sp}$; therefore, the required condition is that $U(z) \leq 0$ for $0 \leq z \leq z_{sp}$. To satisfy this condition, $U(z_{sp}) \leq 0$ is necessary. $U(z_{sp}) \leq 0$ can be rewritten using a parabola in the initial velocity plane v_{yd0}-v_{zd0}

$$v_{yd0} \geq -\frac{m}{eb}z_{sp}^{-2}v_{zd0}^2 + \frac{1}{4}\frac{eb}{m}z_{sp}^2 + 2\frac{B_g}{bz_{sp}}v_{xd0} + \frac{eB_g}{m}\frac{B_g}{b}, \tag{A3}$$

and we can consider the mapping between the v_{yd0}-v_{zd0} plane and the v_y-v_z plane. If particles are on this parabola at $t = 0$ at $z = 0$, which means $U(z_{sp}) = 0$, these particles are mapped into $v_z = v_{zd} = 0$ in the v_y-v_z plane at $z = z_{sp}$, and to left of the parabola by Eq. (5). See also Fig. 3(b) in Ref. 2, green segments in that figure represent the mapping. The parabola of Eq. (5) itself is mapped from the particles on the line $v_{zd0} = 0$ in the right of the v_{yd0}-intercept of Eq. (A3). See the yellow segments in Fig. 3(b) in Ref. 2. If $U(z)$ is a monotonically increasing function of z in the range of $0 \leq z \leq z_{sp}$ and if $v_{zd0} > 0$, which gives $U(0) = -v_{zd0}^2 < 0$, particles can reach $z = z_{sp}$ without reflection as long as $U(z_{sp}) \leq 0$, equivalently, Eq. (A3). In this case, $v_{zd0} > 0$ and $U(z_{sp}) \leq 0$ mean that particles satisfy the inequality Eq. (A3), but not on the $v_{zd0} = 0$ line, and the mapped particles should be to the left of the parabola by (5), which are not related to the crescent boundary parabola. Therefore, to discuss the value of c_z, we need to consider the condition that $U(z)$ is not a monotonically increasing function but has an extremum value in $0 \leq z \leq z_{sp}$. In that case, $U(z_{sp}) \leq 0$ is a necessary condition but not a sufficient condition to satisfy $U(z) \leq 0$ in $0 \leq z \leq z_{sp}$. In the following, we will consider the conditions to satisfy $U(z) \leq 0$ in $0 \leq z \leq z_{sp}$.

Case 1: when $v_{xd0} < 0$

$dU(z)/dz = 0$ occurs only at a single point in $z > 0$ or at two points in $z < 0$ and at a single point in $z > 0$. In both cases, $U(z)$ has a single minimum in $z > 0$. Therefore, as long as $v_{zd0} \geq 0$ and $U(z_{sp}) \leq 0$, particles can reach $z = z_{sp}$. Hence, the value $c_z = 0$; in other words, the condition is $v_{zd0}^2 \geq c_z = 0$.

Case 2: when $v_{xd0} \geq 0$

Published under license by AIP Publishing

(i) when $v_{yd0} - (eB_g/m)(B_g/b) \le 0$
$dU(z)/dz = 0$ occurs only at a single point in $z \le 0$, and the potential $U(z)$ is increasing in $0 \le z \le z_{sp}$. Therefore, the particles with $v_{yd0} - (eB_g/m)(B_g/b) \le 0$ are not related to the crescent boundary.

(ii) when $v_{yd0} - (eB_g/m)(B_g/b) > 0$
$U(z)$ has two inflection points, where $d^2U(z)/dz^2 = 0$, and which are given as follows:

$$z_{\pm} = \pm\left[\frac{2}{3}\frac{m}{eb}\left(v_{yd0} - \frac{eB_g}{m}\frac{B_g}{b}\right)\right]^{1/2}. \tag{A4}$$

We will consider the following three cases.

(ii-A) when $dU(z)/dz = 0$ has only one solution:
If $dU(z_+)/dz > 0$; i.e., if $(3/2)[(eB_g/m)(B_g/b)]^{1/3}v_{xd0}^{2/3} > v_{yd0} - (eB_g/m)(B_g/b)$, the derivative of potential $dU(z)/dz$ becomes zero only at a single point in $z < 0$. In this case, the situation is the same as case (i), and particles are not related to the crescent boundary.
(ii-B) when $dU(z)/dz = 0$ has two solutions:
If $dU(z_+)/dz = 0$, i.e., if $(3/2)[(eB_g/m)(B_g/b)]^{1/3}v_{xd0}^{2/3} = v_{yd0} - (eB_g/m)(B_g/b)$, the potential $U(z)$ is increasing in $0 \le z \le z_{sp}$, even though $dU(z)/dz$ becomes zero at $z = z_+ > 0$. Therefore, particles are not related to the crescent boundary.
(ii-C) when $dU(z)/dz = 0$ has three solutions:
If $dU(z_+)/dz < 0$; i.e., $(3/2)[(eB_g/m)(B_g/b)]^{1/3}v_{xd0}^{2/3} < v_{yd0} - (eB_g/m)(B_g/b)$, the potential $U(z)$ has three extremum points, say, $z = z_1$, $z = z_2$, and $z = z_3$, assuming $z_1 < z_2 < z_3$, which are the solutions of $dU(z)/dz = 0$.

If $z_{sp} \le z_2$, $U(z)$ is increasing in the range $0 \le z \le z_{sp}$. In that case, particles in this condition are not related to the crescent boundary.

If $z_2 < z_{sp}$, $U(z_2) \le 0$ and $U(z_{sp}) \le 0$ are the required conditions for particles to reach $z = z_{sp}$. From $U(z_2) \le 0$, we have the value of c_z as follows:

$$c_z = \frac{1}{4}\left(\frac{eb}{m}\right)^2 z_2^4 - \left(\frac{eb}{m}\right)\left(v_{yd0} - \frac{eB_g}{m}\frac{B_g}{b}\right)z_2^2 + 2\frac{eB_g}{m}v_{xd0}z_2. \tag{A5}$$

In conclusion, from the above discussions of case 1 and case 2, we only need to consider the condition $v_{zd0}^2 > c_z$ with Eq. (A5), for $v_{xd0} \ge 0$.

Let us see the correction for the intercept of Eq. (5) by c_z in Eq. (A5). Rigorously speaking, the solution $z = z_2$ is a function of v_y and v_x, and we need to solve Eq. (5) simultaneously with Eq. (A5); however, assuming that the correction due to c_z is the secondary effect, we can estimate the correction term by substituting the leading order values of v_y and v_x into Eq. (A5). For example, let us examine the crescent curve in Fig. 3(d), the cut of VDF for run 2 ($B_G = 0.2B_0$) at the $v_x = 4v_A$ plane at $z = z_X + 0.45d_i$. Using the parameters in Table I, and $z = 0.4d_i$, we compute the correction for the v_y-intercept, $-(m/eb)z^{-2}c_z$. To compute c_z, let us use the v_y-intercept of the parabola Eq. (5) in Fig. 3(d), $v_y = -0.12v_A$, at the left tip of the magenta curve. Using Eqs. (1) and (2), and $v_{xd} = v_x + kz_c/B_g$ and $v_{yd} = v_y + k/b$, we can obtain the solutions of $dU(z)/dz = 0$ numerically. Using the second largest solution, $z = z_2$, we obtain c_z from Eq. (A5). The correction due to c_z is $-(m/eb)z^{-2}c_z = -0.09v_A$, and this is negligibly small. Therefore, Eq. (5), which is obtained by neglecting c_z, is practically valid to discuss the boundaries of VDFs.

APPENDIX B: CRESCENT CURVE IN $v_{\perp 1}$-$v_{\perp 2}$ FOR $x = x_r > 0$

Equation (31) represents a crescent boundary curve in the $v_{\perp 1}$-$v_{\perp 2}$ plane for $x = x_r > 0$, expressed using v_y in Eq. (17). We can derive an alternative equation for the same boundary curve, directly converting (v_x, v_y, v_z) in Eq. (5) and Eq. (11) into $(v_\parallel, v_{\perp 1}, v_{\perp 2})$, and eliminating $v_\parallel$ from the two converted equations. Using Eqs. (29) and (30), and rewriting v_{xr}, v_{yr}, and v_z as $v_\parallel$, $-v_{\perp 1}$ and $-v_{\perp 2}$, respectively, we obtain the following two converted equations from Eqs. (5) and (11):

$$v_\parallel \sin\theta - v_{\perp 1}\cos\theta = \frac{m}{eb}z_{sp}^{-2}v_{\perp 2}^2 - \frac{1}{4}\frac{eb}{m}z_{sp}^2 - \frac{k}{b} + 2\frac{B_g}{bz_{sp}} \times \left(v_\parallel \cos\theta + v_{\perp 1}\sin\theta\right) + \frac{2kz_c}{bz_{sp}} - \frac{eB_g}{m}\frac{B_g}{b}, \tag{B1}$$

$$\left(v_\parallel \sin\theta - v_{\perp 1}\cos\theta\right)^2 + v_{\perp 2}^2 = s^{-2}\left[v_\parallel \cos\theta + v_{\perp 1}\sin\theta - sv_0 - (s^2+1)\frac{eB_g}{m}z_{sp}\right]^2 + \phi - (s^2+1)\left(\frac{eB_g}{m}z_{sp}\right)^2 - 2sv_0\frac{eB_g}{m}z_{sp}, \tag{B2}$$

where we changed the inequality in Eq. (5) to the equality, and used $z = z_{sp}$. If we eliminate $v_\parallel$ from those two equations, the boundary of the reduced VDF in the $v_{\perp 1}$-$v_{\perp 2}$ plane is obtained. The result is given as follows:

$$v_{\perp 1} = \frac{-A_1' + (A_1'^2 - A_0'A_2')^{1/2}}{A_0'}, \tag{B3}$$

where A_0', A_1', and A_2' are

$$A_0' = \left[1 - 4s^2\left(\frac{B_g}{bz}\right)^2\right], \tag{B4}$$

$$A_1' = -\left(-\frac{m}{eb}z_{sp}^{-2}v_{\perp 2}^2 + \frac{1}{4}\frac{eb}{m}z_{sp}^2 + \frac{k}{b} - 2\frac{k}{b}\frac{z_c}{z_{sp}} + \frac{eB_g}{m}\frac{B_g}{b}\right) \times \left(\cos\theta - 2s^2\frac{B_g}{bz_{sp}}\sin\theta\right) + \left[sv_0 + (s^2+1)\frac{eB_g}{m}z_{sp}\right]\left(2\frac{B_g}{bz_{sp}}\cos\theta - \sin\theta\right), \tag{B5}$$

$$A_2' = \left\{\left(-\frac{m}{eb}z_{sp}^{-2}v_{\perp 2}^2 + \frac{1}{4}\frac{eb}{m}z_{sp}^2 + \frac{k}{b} - 2\frac{k}{b}\frac{z_c}{z_{sp}} + \frac{eB_g}{m}\frac{B_g}{b}\right)\cos\theta - \left[sv_0 + (s^2+1)\frac{eB_g}{m}z_{sp}\right]\left(2\frac{B_g}{bz_{sp}}\cos\theta - \sin\theta\right)\right\}^2 - s^2\left(2\frac{B_g}{bz_{sp}}\cos\theta - \sin\theta\right)^2\left[2s\frac{eB_g}{m}z_{sp}v_0 + (s^2+1)\left(\frac{eB_g}{m}\right)^2 z_{sp}^2 - \phi + v_{\perp 2}^2\right] - s^2\left(-\frac{m}{eb}z_{sp}^{-2}v_{\perp 2}^2 + \frac{1}{4}\frac{eb}{m}z_{sp}^2 + \frac{k}{b} - 2\frac{k}{b}\frac{z_c}{z_{sp}} + \frac{eB_g}{m}\frac{B_g}{b}\right)^2 \sin^2\theta. \tag{B6}$$

Published under license by AIP Publishing

Equation (B3) looks more complex than Eq. (31), but they actually represent the same curve. We numerically verified that both Eq. (B3) and Eq. (31) give the same curve.

REFERENCES

[1]M. Hesse, N. Aunai, D. Sibeck, and J. Birn, "On the electron diffusion region in planar, asymmetric, systems," Geophys. Res. Lett. **41**, 8673, https://doi.org/10.1002/2014GL061586 (2014).

[2]N. Bessho, L.-J. Chen, and M. Hesse, "Electron distribution functions in the diffusion region of asymmetric magnetic reconnection," Geophys. Res. Lett. **43**, 1828, https://doi.org/10.1002/2016GL067886 (2016).

[3]L.-J. Chen, M. Hesse, S. Wang, N. Bessho, and W. Daughton, "Electron energization and structure of the diffusion region during asymmetric reconnection," Geophys. Res. Lett. **43**, 2405, https://doi.org/10.1002/2016GL068243 (2016).

[4]M. A. Shay, T. D. Phan, C. C. Haggerty, M. Fujimoto, J. F. Drake, K. Malakit, P. A. Cassak, and M. Swisdak, "Kinetic signatures of the region surrounding the X line in asymmetric (magnetopause) reconnection," Geophys. Res. Lett. **43**, 4145, https://doi.org/10.1002/2016GL069034 (2016).

[5]G. Lapenta, J. Berchem, M. Zhou, R. J. Walker, M. El-Alaoui, M. L. Goldstein, W. R. Paterson, B. L. Giles, C. J. Pollock, C. T. Russell, R. J. Strangeway, R. E. Ergun, Y. V. Khotyaintsev, R. B. Torbert, and J. L. Burch, "On the origin of the crescent-shaped distributions observed by MMS at the magnetopause," J. Geophys. Res. **122**, 2024, https://doi.org/10.1002/2016JA023290 (2017).

[6]N. Bessho, L.-J. Chen, M. Hesse, and S. Wang, "The effect of reconnection electric field on crescent and U-shaped distribution functions in asymmetric reconnection with no guide field," Phys. Plasmas **24**, 072903 (2017).

[7]S. Zenitani, H. Hasegawa, and T. Nagai, "Electron dynamics surrounding the X line in asymmetric magnetic reconnection," J. Geophys. Res. **122**, 7396, https://doi.org/10.1002/2017JA023969 (2017).

[8]P. A. Cassak, K. J. Genestreti, J. L. Burch, T.-D. Phan, M. A. Shay, M. Swisdak, J. F. Drake, L. Price, S. Eriksson, R. E. Ergun, B. J. Anderson, V. G. Merkin, and C. M. Komar, "The effect of a guide field on local energy conversion during asymmetric magnetic reconnection: Particle-in-cell simulations," J. Geophys. Res. **122**, 11523, https://doi.org/10.1002/2017JA024555 (2017).

[9]J. L. Burch, R. B. Torbert, T. D. Phan, L.-J. Chen, T. E. Moore, R. E. Ergun, J. P. Eastwood, D. J. Gershman, P. A. Cassak, M. R. Argall, S. Wang, M. Hesse, C. J. Pollock, B. L. Giles, R. Nakamura, B. H. Mauk, S. A. Fuselier, C. T. Russell, R. J. Strangeway, J. F. Drake, M. A. Shay, Yu. V. Khotyaintsev, P.-A. Lindqvist, G. Marklund, F. D. Wilder, D. T. Young, K. Torkar, J. Goldstein, J. C. Dorelli, L. A. Avanov, M. Oka, D. N. Baker, A. N. Jaynes, K. A. Goodrich, I. J. Cohen, D. L. Turner, J. F. Fennell, J. B. Blake, J. Clemmons, M. Goldman, D. Newman, S. M. Petrinec, K. J. Trattner, B. Lavraud, P. H. Reiff, W. Baumjohann, W. Magnes, M. Steller, W. Lewis, Y. Saito, V. Coffey, and M. Chandler, "Electron-scale measurements of magnetic reconnection in space," Science **352**, aaf2939 (2016).

[10]L.-J. Chen, M. Hesse, S. Wang, D. Gershman, R. Ergun, C. Pollock, R. Torbert, N. Bessho, W. Daughton, J. Dorelli, B. Giles, R. Strangeway, C. Russell, Y. Khotyaintsev, J. Burch, T. Moore, B. Lavraud, T. Phan, and L. Avanov, "Electron energization and mixing observed by MMS in the vicinity of an electron diffusion region during magnetopause reconnection," Geophys. Res. Lett. **43**, 6036, https://doi.org/10.1002/2016GL069215 (2016).

[11]T. D. Phan, J. P. Eastwood, P. A. Cassak, M. Øieroset, J. T. Gosling, D. J. Gershman, F. S. Mozer, M. A. Shay, M. Fujimoto, W. Daughton, J. F. Drake, J. L. Burch, R. B. Torbert, R. E. Ergun, L. J. Chen, S. Wang, C. Pollock, J. C. Dorelli, B. Lavraud, B. L. Giles, T. E. Moore, Y. Saito, L. A. Avanov, W. Paterson, R. J. Strangeway, C. T. Russell, Y. Khotyaintsev, P. A. Lindqvist, M. Oka, and F. D. Wilder, "MMS observations of electron-scale filamentary currents in the reconnection exhaust and near the X line," Geophys. Res. Lett. **43**, 6060, https://doi.org/10.1002/2016GL069212 (2016).

[12]C. Norgren, D. B. Graham, Yu. V. Khotyaintsev, M. André, A. Vaivads, L.-J. Chen, P.-A. Lindqvist, G. T. Marklund, R. E. Ergun, W. Magnes, R. J. Strangeway, C. T. Russell, R. B. Torbert, W. R. Paterson, D. J. Gershman, J. C. Dorelli, L. A. Avanov, B. Lavraud, Y. Saito, B. L. Giles, C. J. Pollock, and J. L. Burch, "Finite gyroradius effects in the electron outflow of asymmetric magnetic reconnection," Geophys. Res. Lett. **43**, 6724, https://doi.org/10.1002/2016GL069205 (2016).

[13]J. L. Burch and T. D. Phan, "Magnetic reconnection at the dayside magnetopause: Advances with MMS," Geophys. Res. Lett. **43**, 8327, https://doi.org/10.1002/2016GL069787 (2016).

[14]L.-J. Chen, M. Hesse, S. Wang, D. Gershman, R. E. Ergun, J. Burch, N. Bessho, R. B. Torbert, B. Giles, J. Webster, C. Pollock, J. Dorelli, T. Moore, W. Paterson, B. Lavraud, R. Strangeway, C. Russell, Y. Khotyaintsev, P.-A. Lindqvist, and L. Avanov, "Electron diffusion region during magnetopause reconnection with an intermediate guide field: Magnetospheric multiscale observations," J. Geophys. Res. **122**, 5235, https://doi.org/10.1002/2017JA024004 (2017).

[15]K. J. Genestreti, J. L. Burch, P. A. Cassak, R. B. Torbert, R. E. Ergun, A. Varsani, T. D. Phan, B. L. Giles, C. T. Russell, S. Wang, M. Akhavan-Tafti, and R. C. Allen, "The effect of a guide field on local energy conversion during asymmetric magnetic reconnection: MMS observations," J. Geophys. Res. **122**, 11342, https://doi.org/10.1002/2017JA024247 (2017).

[16]M. R. Argall, K. Paulson, L. Alm, A. Rager, J. Dorelli, J. Shuster, S. Wang, R. B. Torbert, H. Vaith, I. Dors, M. Chutter, C. Farrugia, J. Burch, C. Pollock, B. Giles, D. Gershman, B. Lavraud, C. T. Russell, R. Strangeway, W. Magnes, P.-A. Lindqvist, Yu. V. Khotyaintsev, R. E. Ergun, and N. Ahmadi, "Electron dynamics within the electron diffusion region of asymmetric reconnection," J. Geophys. Res. **123**, 146, https://doi.org/10.1002/2017JA024524 (2018).

[17]A. C. Rager, J. C. Dorelli, D. J. Gershman, V. Uritsky, L. A. Avanov, R. B. Torbert, J. L. Burch, R. E. Ergun, J. Egedal, C. Schiff, J. R. Shuster, B. L. Giles, W. R. Paterson, C. J. Pollock, R. J. Strangeway, C. T. Russell, B. Lavraud, V. N. Coffey, and Y. Saito, "Electron crescent distributions as a manifestation of diamagnetic drift in an electron-scale current sheet: Magnetospheric multiscale observations using new 7.5 ms Fast Plasma Investigation moments," Geophys. Res. Lett. **45**, 578, https://doi.org/10.1002/2017GL076260 (2018).

[18]K. J. Genestreti, A. Varsani, J. L. Burch, P. A. Cassak, R. B. Torbert, R. Nakamura, R. E. Ergun, T. D. Phan, S. Toledo-Redondo, M. Hesse, S. Wang, B. L. Giles, C. T. Russell, Z. Vörös, K.-J. Hwang, J. P. Eastwood, B. Lavraud, C. P. Escoubet, R. C. Fear, Y. Khotyaintsev, T. K. M. Nakamura, J. M. Webster, and W. Baumjohann, "MMS observation of asymmetric reconnection supported by 3-D electron pressure divergence," J. Geophys. Res. **123**, 1806, https://doi.org/10.1002/2017JA025019 (2018).

[19]M. Hesse, Y.-H. Liu, L.-J. Chen, N. Bessho, M. Kuznetsova, J. Birn, and J. L. Burch, "On the electron diffusion region in asymmetric reconnection with a guide magnetic field," Geophys. Res. Lett. **43**, 2359, https://doi.org/10.1002/2016GL068373 (2016).

[20]M. Hesse, L.-J. Chen, Y.-H. Liu, N. Bessho, and J. L. Burch, "Population mixing in asymmetric magnetic reconnection with a guide field," Phys. Rev. Lett. **118**, 145101 (2017).

[21]M. Hesse, N. Aunai, S. Zenitani, M. Kuznetsova, and J. Birn, "Aspects of collisionless magnetic reconnection in asymmetric systems," Phys. Plasmas **20**, 061210 (2013).

[22]J. Egedal, A. Le, W. Daughton, B. Wetherton, P. A. Cassak, L.-J. Chen, B. Lavraud, R. B. Torbert, J. Dorelli, D. J. Gershman, and L. A. Avanov, "Spacecraft observations and analytic theory of crescent-shaped electron distributions in asymmetric magnetic reconnection," Phys. Rev. Lett. **117**, 185101 (2016).

[23]B. U. Ö. Sonnerup and M. Scheible, "Minimum and maximum variance analysis," in *Analysis Methods for Multi-Spacecraft Data, ISSI. Sci. Rep. SR-001*, edited by G. Paschmann and P. W. Daly (ESA PublICATION, 1998), pp. 185–220.

Published under license by AIP Publishing